Lawrence Berkeley National Laboratory
Recent Work

Title
MODULATED STRUCTURES AND COARSENING IN ORDERED (Cu-Mn)3Al ALLOYS

Permalink
https://escholarship.org/uc/item/5nh7p14s

Authors
Bouchard, M.
Thomas, G.

Publication Date
1973-11-01

eScholarship.org Powered by the California Digital Library
University of California

RECEIVED
LAWRENCE
RADIATION LABORATORY

APR 19 1974

LIBRARY AND
DOCUMENTS SECTION

LBL-2294
Preprint

MODULATED STRUCTURES AND COARSENING IN ORDERED $(Cu\text{-}Mn)_3Al$ ALLOYS

M. Bouchard and G. Thomas

November 1973

Prepared for the U. S. Atomic Energy Commission
under Contract W-7405-ENG-48

TWO-WEEK LOAN COPY

This is a Library Circulating Copy which may be borrowed for two weeks. For a personal retention copy, call Tech. Info. Division, Ext. 5545

LAWRENCE BERKELEY LABORATORY
UNIVERSITY OF CALIFORNIA

LBL-2294
Preprint

DISCLAIMER

This document was prepared as an account of work sponsored by the United States Government. While this document is believed to contain correct information, neither the United States Government nor any agency thereof, nor the Regents of the University of California, nor any of their employees, makes any warranty, express or implied, or assumes any legal responsibility for the accuracy, completeness, or usefulness of any information, apparatus, product, or process disclosed, or represents that its use would not infringe privately owned rights. Reference herein to any specific commercial product, process, or service by its trade name, trademark, manufacturer, or otherwise, does not necessarily constitute or imply its endorsement, recommendation, or favoring by the United States Government or any agency thereof, or the Regents of the University of California. The views and opinions of authors expressed herein do not necessarily state or reflect those of the United States Government or any agency thereof or the Regents of the University of California.

MODULATED STRUCTURES AND COARSENING IN ORDERED $(Cu-Mn)_3Al$ ALLOYS

M. Bouchard* and G. Thomas

Department of Materials Science and Engineering, College of Engineering; and Inorganic Materials Research Division, Lawrence Berkeley Laboratory, University of California, Berkeley, California 94720.

ABSTRACT

Quenched and aged alloys along the composition line Cu_3Al-Cu_2MnAl have been studied by electron diffraction and microscopy. During the quench, ordering occurs producing an ordered solid solution based on the DO_3 structure of Cu_3Al and the $L2_1$ structure of Cu_2MnAl.

Upon isothermal aging at temperatures below 350°C, decomposition occurs inside a miscibility gap into a Cu_2MnAl-rich phase and a Cu_3Al-rich phase. The microstructures possess all the metallographic characteristics of a spinodal decomposition. The early stage of the decomposition is characterized by composition modulations having a range of wavevectors close to <100>. The wavelength developes into resolvable values of 40-100Å and gradually increases with aging time.

During isothermal aging of the symmetrical alloy at temperatures just below the miscibility gap, a complex microstructure consisting of widely different wave lengths developes. At this stage, rod-like particles of the Cu_2MnAl-rich phase having the $L2_1$ structure are coherent with those of the Cu_3Al phase having a tetragonal structure. In Mn-rich asymmetrical alloys, the Cu_3Al-rich minor phase has a plate-like morphology whereas in the Al-rich asymmetrical alloy, the Cu_2MnAl-rich minor phase heterogeneously nucleates at 1/4 a<111> APB's.

---

* Present Address: Communication Research Center, P.O. Box 490, Station A, Ottawa, Canada

During prolonged aging of the symmetrical alloy at temperatures just below the miscibility gap, the interfacial coherency strains are eventually relieved and the Cu_3Al-rich phase returns to its DO_3 cubic symmetry.

1. INTRODUCTION

The metallography of the Cu-rich portion of the Cu-Mn-Al system has been fully investigated by West and Thomas[1] at temperatures above 450°C. They found that the addition of Mn expands the high temperature β phase field of the Cu-Al system. The compositional range of stability of the β phase increases with temperature, and includes the composition of the well known Heusler alloy Cu_2MnAl at temperatures above 650°C. At 400°C, the equilibrium phases in this alloy are: Cu_3Mn_2Al, γ and β_{Mn}. The precipitation of these phases can be suppressed by quenching (1-6). The high temperature β phase has a disordered bcc structure which orders rapidly during quenching. The ordering takes place in two stages [4,5,6], forming first the B2 structure at T_cB2 and the $L2_1$ structure at T_cL2_1. The highest ordering temperatures of the ternary alloys are found near the stoichiometric composition Cu_2MnAl of the Heusler alloy (T_cB2 = 750-770°C and T_cL2_1 = 615°C).

The low temperature aging characteristics of the ternary alloys are strongly influenced by their compositions. In the stoichiometric alloy, Cu_2MnAl, the ordered $L2_1$ structure of the as-quenched alloy is stabilized during aging below 325°C[2,7]. In non-stoichiometric alloys aged in the same temperature range, the precipitation of other phases has been reported[2,7,8,9,11].

The alloys along the composition line Cu_3Al - Cu_2MnAl are of particular interest since the $L2_1$ structure of the Cu_2MnAl alloy resembles very closely the DO_3 structure of the binary Cu_3Al alloy, and the difference between their lattice parameters is only about 2% (a = 5.95Å and 5.83Å respectively)[8,10,11]. An x-ray diffraction study by Johnston and Hall[2] of an alloy near $Cu_{2.5}Mn_{0.5}Al$ (half way between Cu_3Al and Cu_2MnAl) showed the presence of satellite lines after brief aging at 200°C and a double cubic structure after prolonged aging at 300°C. They interpreted their results in terms of composition modulations forming zones of Cu_2MnAl coherent with a "residue". However, in an earlier x-ray investigation, Persson[11] discovered that aging of the $(Cu\text{-}Mn)_3Al$ alloys resulted in the spearation of two cubic phases that could be interpreted as Cu_3Al and Cu_2MnAl.

The aim of this work was to study in more detail the structure and morphologies of alloys along the composition line Cu_3Al-Cu_2MnAl using electron diffraction and microscopy.

2. EXPERIMENTAL

The alloys studied can be represented by $Cu_{3-x}Mn_xAl$ with $0<x<1$. In the text, the alloys are designated by the x values (x = 0 for Cu_3Al and x = 1 for Cu_2MnAl). Table 1 summarizes the compositions of the alloys studied.

The alloys were prepared by melting high purity elements: 99.999% Cu, 99.9% Mn and 99.999% Al in an induction furnace under a helium atmosphere and were chill cast into a copper mold. Chemical analysis verified to within 1 weight % the compositions given in Table 1.

TABLE 1

Atomic and chemical compositions of the alloys studied. The value of X represents the atomic fraction of Mn in the alloys and is used in the text to designate the alloys.

Atomic Composition	Estimated Composition wt % Cu	wt % Mn	wt % al	X
Cu_3Al	87.6	---	12.4	0
$Cu_{2.8}Mn_{0.2}Al$	82.4	5.1	12.5	0.2
$Cu_{2.5}Mn_{0.5}Al$	74.3	13.1	12.6	0.5
$Cu_{2.2}Mn_{0.8}Al$	66.4	20.8	12.8	0.8
$Cu_{2.1}Mn_{0.9}Al$	63.5	23.6	12.9	0.9
Cu_2MnAl	60.9	26.2	12.9	1.0

The ingots were then placed in stainless steel envelopes, homogenized for three days at 850°C and oil quenched in order to avoid quenching cracks. Thin slices, 0.5mm thick, were then cut and homogenized at 850°C for 10 min. in a vertical resistance air furnace. They were then quenched in iced brine to avoid precipitation of the high temperature phases and also to minimize the decomposition of the alloys inside the miscibility gap that exists at temperatures below 350°C. The alloys were then aged for various times in the temperature range of 200°C to 370°C. The aging treatments were carried out in oil baths at temperatures below 250°C and in salt baths (50% potassium nitrate - 50% sodium nitrate) above 250°C.

Electron microscope disc specimens, 2.3mm in diameter, were spark eroded from the heat treated discs and thinned in an automatic jet

polisher[12] using the chromic-acetic acid electrolyte. The thin discs were examined in a Siemens Elmiskop IA microscope operating at 100 kV.

3. CRYSTALLOGRAPHY OF THE $(Cu-Mn)_3Al$ ALLOYS

The alloys along the composition line Cu_3Al-Cu_2MnAl order in two stages during the quench. The ordering sequence of the middle alloy 0.5 is shown schematically in Fig. 1. The high temperature bcc disordered structure of the β phase orders first to the B2 structure. At lower temperatures, the B2 structure further orders. This ordering is equivalent to the well documented[13] B2→DO_3 ordering in A_3B alloys and the B2→$L2_1$ ordering in A_2BC alloys. The B2 structure of the $(Cu-Mn)_3Al$ alloys transforms to an ordered solid solution (DO_3-$L2_1$) based on the DO_3 structure of Cu_3Al and the closely related $L2_1$ structure of Cu_2MnAl. The DO_3 and $L2_1$ superstructures consist of four interpenetrating fcc sublattices. Two of the fcc sublattices are occupied by Cu atoms (the unmarked corner sites in Fig. 1) and the third sublattice (Δ) is occupied by Al atoms. The fourth sublattice is occupied by a random mixture of the remaining Cu and Mn atoms and its composition is determined by the composition of the alloy. In alloys along the tie-line Cu_3Al-Cu_2MnAl, the composition of the fourth sublattice gradually changes from Cu to Mn. Ordering of the Cu and Mn atoms occupying the fourth sublattice has not yet been detected in diffraction patterns. Decomposition of the single phase ordered solid solution (DO_3-$L2_1$) into a two phase mixture of Cu_3Al-rich DO_3 regions and Cu_2MnAl-rich $L2_1$ regions is accomplished solely by the decomposition of the fourth sublattice into a Cu-rich sublattice and a Mn-rich sublattice (Fig. 1).

There are two possible types of APB vectors in the DO_3 and the $L2_1$ structure. The 1/4a<111> and the 1/2a<100> APB vectors are shown in Fig. 1.

4. EXPERIMENTAL RESULTS

4.1 Ordering Temperatures

Thermal analysis was carried out in order to determine the two ordering temperatures of the alloys and the results are summarized in Fig. 2. The results for the Cu_2MnAl alloy are comparable to those obtained by other workers[4,5,6]. Two thermal arrests of different magnitudes were observed in alloys having an atomic fraction of Mn $x \geq 0.5$ and they are associated with $T_c B2$ and $T_c L2_1$. The magnitude of the thermal arrest associated with the B2 ordering reaction increases with the Mn content. In the alloys $x \leq 0.2$, the thermal arrest associated with the B2 ordering reaction was too small to be observed. In the Cu_2Al alloy ($x = 0$), in addition to the B2→$L2_1$ thermal arrest, a second thermal arrest was observed at 350°C and this corresponds to the M_s temperature in this alloy[14].

4.2 The As-quenched Alloys

Two types of microstructures have been observed in quenched $(Cu\text{-}Mn)_3Al$ alloys; those containing martensite and those containing the untransformed ordered β phase. The martensitic phases of the binary Cu-Al system are well documented[14-15]. It was found that the M_s temperature of the Cu_3Al alloy gradually decreases by the addition of Mn. Isolated martensite plates were observed in the as-quenched alloy 0.2, but not in the as-quenched alloy 0.5. The martensitic transformation in these alloys will be the subject of another paper.

After quenching, the non martensitic alloys possess a "tweed-like" microstructure and correspondingly, their diffraction patterns show diffuse scattering. The contrast of the "tweed-like" microstructure and the intensity of diffuse scattering decrease with the Mn content of the alloys. Typical examples are shown in the micrograph and diffraction pattern of the as-quenched symmetrical alloy ($x = 0.5$) in Fig. 3. This behaviour is similar to that of many age-hardenable alloy systems and suggests the presence of dense array of fine coherent precipitates exhibiting strain contrast, which form during the quench.

4.3 Early Growth

It was found that the alloys briefly aged inside the miscibility gap decompose by forming composition modulations parallel to the cube planes of the matrix. Evidence of the decomposition appears first in diffraction patterns. Fig. 4(a) and (b) shows part of the 001 diffraction pattern of the alloys 0.5 and 0.8 respectively after aging at 200°C for various times indicated in minutes. Clearly, during aging of the two alloys for times less than 4 min., the decomposition produces diffuse intensity in the shape of an heraldic cross patée around all reflections in the (001) diffraction patterns. The arms of the crosses tend to lie parallel to the cube directions of the matrix. This geometry is believed to arise from a range of compositional wave lengths having wave vectors near the <100> directions. This behaviour is characteristic of a spinodal decomposition, but could also result from a regular array of homogeneously nucleated precipitates.

During further aging, well defined satellites are observed to develop from the diffuse cross patée (see Fig. 4). This is thought to

arise from the preferential growth of a critical compositional wave length λ from the range of initial λ's. In addition, Fig. 4 shows that the satellite spacing decreases as the aging time increases from two minutes to two hours. This reflects a gradual increase in the compositional wave length λ with aging time.

The (001) reciprocal lattice plane shows two satellite pairs along [100] and [010] resulting from the growth of λ in the [100] and [010] directions respectively. In <111> oriented foils, the three pairs of satellites can be concurrently observed. (111) diffraction patterns of the alloy 0.5 aged at 200°C for 15 min. and at 300°C for 30 sec. are shown in Fig. 5(a) and (b) respectively. Allowing for the small curvature of the reflecing sphere, the distribution of intensity of satellites at 200°C appears to be symmetrical, whereas at 300°C the distribution is asymmetrical. This suggests that at 200°C, the three <100> directions of growth are equally favored whereas at 300°C, there exists a preferential growth along one or two <100> growth directions.

The wave length of the early stage of the decomposition can be estimated using the intersatellite spacing in diffraction patterns, which averages the wave lengths from the area selected, or by direct measurements of interparticle spacings in images[17, 18]. The latter method requires accurate calibrations of magnifications whereas the former method is independent of magnification. A sequence of bright field images showing the gradual increase in λ during the early stages of the decomposition and evidence for antiphase domain boundaries (APB's), is shown in Fig. 6. The fringe contrast at APB's was also observed in the as-quenched alloys indicating that the ordering precedes the modulated

decomposition. The modulated microstructure was also observed to exist up to the grain boundaries (Fig. 7) indicating the homogeneous nature of the transformation.

The kinetics of the early growth of the wave length were measured in the alloy 0.5 in the temperature range of 200°C to 300°C. The results are summarized in the log λ vs log t plot in Fig. 8 where the value of λ was calculated from at least ten independent diffraction patterns. The most probable error for each measurement is also indicated. The relationship between log λ and log t is linear and can be represented by:

$$\lambda = kt^n \qquad (1)$$

The values of n (the slopes of the lines in Fig. 8) were calculated using the method of least squares for nonlinear equations described by Southworth and Deleeuw[19]. The resulting values are 0.127, 0.172 and 0.216 at 200°C, 240°C and 300°C respectively. These values are somewhat lower than the n = 1/3 value of the theories of coarsening presented by Lifshitz and Slyozov[20] and Wagner[21]. Values of n = 1/3 were obtained during a study of the coarsening of the spinodal microstructure in Cu-Ni-Fe[18] and also during coarsening of the classically nucleated composition modulations in the Ni-Al system[22].

The APBs of the as-quenched alloys were smoothly curved and they remained smoothly curved during brief aging at temperatures well inside the miscibility gap even though the microstructure is modulated. A striking example of this behaviour is shown in Fig. 9 where the smoothly curved APBs and the composition modulations are imaged simultaneously in the alloy 0.5 aged at 300°C for 30 sec. The foil orientation is $[01\bar{1}]$ and the composition modulations parallel to [100] are also parallel to the electron beam. They show greater contrast than those parallel

to [010] and [001] which are oriented at 45° to the electron beam. In this [01$\bar{1}$] orientation, the image of the composition modulations is formed by the (022) fundamental reflection and their image in this (111) superlattice dark field micrograph is caused by double diffraction. The isotropic behaviour of APBs was observed in microstructures aged up to 40 min. at 300°C for which λ (average) $\approx$300Å. It therefore appears that there is little interaction between the APBs and the modulated structure during the early stages of decomposition. This is in contrast to the behaviour in other Cu-Mn-Al alloys where the APBs were found to rapidly migrate to the {001} interface between the $L2_1$ matrix and the small plate-like bcc disordered precipitates[7].

4.4 Coarsening

The mean wave length of the decomposition products continues to increase during further aging inside the miscibility gap. Typical coherent microstructures obtained from the alloy 0.5 aged at 300°C for 1,400 min. and 2,000 min. are shown in Fig. 10(a) and (b) respectively where one component has been preferentially thinned during electropolishing. In this symmetrical alloy (alloy having equal fractions of the two phases), the decomposition results in coherent rod-like particles with their long axes parallel to <100> directions. In the microstructure in (a), the rods are parallel to the [010] direction and also parallel to the foil surface (001). In (b), the particles are oriented at 45° to the (011) foil surface and, therefore, they do not appear as long rods. Instead, the electropolishing shortened the rods and they appear as overlapping discs.

The wave lengths were found to vary quite widely during coarsening. For example in Fig. 10(b), regions with wave length of 2,000Å are often separated by regions having an apparent wave length of 150-200Å.

In the asymmetrical alloys 0.8 and 0.9, the minor phase form as thin platelets parallel to the cube planes of the matrix. A typical example from the alloy 0.8 aged at 315°C for 180 min. is shown in Fig. 11. The foil normal is $[1\bar{1}0]$ and, therefore, the platelets parallel to the (001) plane are observed edge on, whereas those parallel to the (100) and (010) planes are oriented at 45° to the foil surface and the interface shows displacement fringe contrast[23].

4.5 Loss of Coherency

During further aging inside the miscibility gap, the two phases lose coherency. In the symmetrical alloy, the loss of coherency occurs at a wave length of about 2,000Å. The fully developed microstructure in Fig. 12 obtained from the alloy 0.5 aged at 300°C for 10,000 min. shows interfacial dislocations. These dislocations have been analysed in a previous paper[24] where it was shown that they are edge in character with Burgers vector of the type a/2<100>. Fig. 12 clearly shows an equiproportion of the two components suggesting that the alloy 0.5 is near the center of the miscibility gap. It can also be seen that component B exhibits a "tweed-like" texture. This feature will be discussed in paper II. The interfacial plate-like precipitates labelled P are analysed in paper III.

The coarsening of microstructures is accompanied by changes in diffraction patterns. This is illustrated in the two (100) diffraction patterns of the alloy 0.5 in Fig. 13(a) and (b) obtained respectively

before and after the loss in coherency. Well before interfacial dislocations were observed, the diffracted spots were elongated and the direction of elongation was always orthogonal to the long axis of the rods in the image. The elongation of the spots increases with g and at large g, the spots were doubled.* No splitting was observed for all g's parallel to the axis of the rods and the splitting was maximum for all g's orthogonal to the long axis of the rods. For simplicity, the magnitude and direction of the splitting are indicated by the magnitude and direction of the arrows in Fig. 13(a). The area marked in Fig. 13(a) is schematically reproduced in Fig. 14(a) and the splitting is interpreted in terms of a two phase microstructure containing a cubic phase and a tetragonal phase. The c/a ratio of the tetragonal phase obtained from measurements from diffraction patterns is 1.033 ± 0.005 with the c axis parallel to the long axis of the rods. The image corresponding to the (100) diffraction pattern in Fig. 14(a) is shown in Fig. 10(a). A dark field experiment has shown that the tetragonal phase contains stacking faults which suggest that it is the Cu_3Al rich phase partially transformed to martensite. All reflections are streaked in the <100> directions viz. the direction of the elastic coherency strains (i.e. in the direction of misfit). The streaks through 000 and 002 type reflections are believed to arise from double diffraction at the coherently strained interface.

After loss of coherency, the streaking is not observed and all spots are doubled with the direction of splitting parallel to the reciprocal lattice vector g. In addition, the magnitude of the splitting increases radially with increasing g. This is clearly shown in Fig. 13(b) where the direction and magnitude of the arrows indicate respectively the

---

* $\vec{g}$ represents a reciprocal lattice vector.

direction and magnitude of the splitting. The area marked in Fig. 13(b) is schematically reproduced in Fig. 14(b) and the splitting is interpreted in terms of two cubic phases. It is, therefore, concluded that after the loss of coherency, both phases are cubic, giving rise to a double cubic structure. The image corresponding to the (100) diffraction pattern in Fig. 14(b) is shown in Fig. 12.

The metastable tetragonal phase observed prior to the loss of coherency must therefore arise from an expansion of the unit cell of the Cu_3Al-rich phase preferentially in the c direction, which is parallel to the long axis of the rods.

The fractional difference in lattice parameter $\Delta a/a$ or the misfit between the two phases can be estimated from the splitting of spots in diffraction patterns such as that shown in Fig. 13(b). In Table 2, this $\Delta a/a$ value is compared to values obtained from the spacing of Moiré fringes observed at the interface and that obtained from the spacing of interfacial dislocations. The $\Delta a/a$ values in Table 2 represent the average values calculated from at least ten measurements on specimen aged at 300°C.

TABLE 2

A comparison of the values of the misfit at 300°C calculated from various sources. * values not corrected for magnification error

	$\Delta a/a$	value obtained from:
a)	1.57% ± 0.15	diffraction patterns
b)	1.78% ± 0.10	Moiré fringes*
c)	1.4% ± 0.30	interfacial dislocations*

The most reliable $\Delta a/a$ value is that obtained from diffraction patterns since it is independent of the magnification error of the microscope. The values in Table 2 are consistent with the presence of a Cu_3Al-rich phase and a Cu_2MnAl-rich phase in the fully developed microstructures.

In asymmetrical alloys, the coherent minor phase has a plate-like morphology (see Fig. 11). Contrast experiments have shown that in the asymmetrical alloys, the interfacial dislocations are similar to those found in the symmetrical alloy[24]. Fig. 15 is a (111) dark field micrograph showing the presence of interfacial dislocations only in certain areas of the interface. In addition, the figure clearly shows that rapid thickening of a plate occurs only near dislocated areas of the interface, (e.g. at X)

The limits of the miscibility gap were estimated using the selected dark field technique and the metallographic features of both phases. The solvus temperatures were taken as the temperatures above which no decomposition of the single phase into the Cu_3Al-rich and the Cu_2MnAl-rich phases was observed after long aging. The results are summarized in Fig. 2 showing the limits of the miscibility gap.

4.6 Nucleation and Growth of Cu_2MnAl-rich particles

Heterogeneous nucleation of Cu_2MnAl precipitates was observed in the binary-rich asymmetrical alloy 0.2 aged at a temperature just below the miscibility gap. This is shown in the micrographs in Fig. 16 obtained from the same area of a foil aged at 240°C for 30 min. The bright field micrographs in (a) shows the early stages of the heterogeneous precipitation. The 1/4a<111> type APB's are in contrast in (b)

whereas, both types of APB's (the 1/4a<111> and the 1/2a<100>) are in contrast in (c). A comparison of the three micrographs shows that the Cu_2MnAl-rich precipitates in (a) nucleate preferentially at 1/4a<111> APBs imaged in (b). The growth of the precipitates is characterized by the formation of rows of cubes parallel to the <100> directions of the matrix as illustrated in Fig. 17. In corresponding diffraction patterns, a doubling of spots was observed, corresponding to a misfit of 2.0% ± 0.3. In addition, the matrix often contained stacking faults. These observations are consistant with the presence of a Cu_3Al-rich matrix and a Cu_2MnAl-rich phase.

5. DISCUSSION

5.1 Spinodal Decomposition

The early stages of the decomposition inside the miscibility gap are metallographically consistent with that expected in the early stages after spinodal decomposition, or a homogeneous phase transformation. The theoretical treatment of spinodal decomposition has been given by Hillert, Hilliard and Cahn and the important features of the transformation have been reviewed by Cahn[25] and more recently by Hilliard[26] and de Fontaine[27].

The structure of the early stages of spinodal decomposition is characterized by sinusoidal composition modulations of wave lengths λ in the unstable single phase. During isothermal aging, the amplitude of the composition modulations increases which results in a uphill diffusion. During the early stage, a range of wave lengths spontaneously decompose and each wave length is characterized by its amplification factor $R(\beta)$. Those having a positive $R(\beta)$ will grow, whereas those having a negative

$R(\beta)$ will decay. The wave length possessing the maximum $R(\beta)$, λ_m eventually emerge from the range of initially present λ's and continues to grow in amplitude.

It is also possible to obtain a highly regular modulated structure by the classical mechanism of nucleation and growth[22]. In this case, a regular array of second phase particles having a well defined composition is homogeneously nucleated from a metastable phase. In contrast to the spinodal mechanism, this results in a downhill diffusion. This is the essential difference between the two mechanisms, and the definitions are purely thermodynamical and cannot be distinguished metallographically. The diffraction effects produced by both mechanisms are also very similar[28] and cannot be distinguished by electron diffraction.

The compositional changes inside the spinodal can be described by a linear diffusion equation. The solution to the linear diffusion equation by Fourrier techniques leads to the expression:

$$A(\beta,t) = A(\beta,o) \exp [R(\beta)t] \qquad (2)$$

where $A(\beta,t)$ is the amplitude of the Fourrier component of wave number β at time t ($\beta = 2\pi/\lambda$ where λ is the wave length) and $R(\beta)$ is the amplification factor[27,27,28].

This equation is only valid during the early stages of the decomposition since in deriving and solving the diffusion equation, it was assumed that all the parameters are independent of composition. At later stages, the large amplitudes of the modulations produce composition gradients, and this approximation is no longer valid. At this stage, the decomposition can be mathematically expressed by a nonlinear diffusion

equation which can be solved by successive approximations[29] or numerically[30]. For discussion of the later stages of the decomposition (see section 5.4), it is useful to identify the following terms of the solution equation in a manner similar to Swanger et al.[30]. The solution equation is composed of a linear term, a nonlinear term and a gradient energy term. The growth of the waves is no longer exponential with time as the solution in equation (2) suggests for the early stage, but the growth is governed by the relative importance of the additional terms in the diffusion equation.

5.2 The Early Stage of the Decomposition

Evidence of the decomposition appears first in diffraction patterns (see Fig. 4). Since the diffraction pattern is a Fourrier transform of the crystal[26,31], the Fourrier spectrum expressed in equation (2) for a modulated structure corresponds to the appearance of diffuse intensity around the transmitted electron beam. By translation of the origin of the reciprocal lattice, the diffuse intensity is expected to appear around all diffracted beams and in fact this is observed in the form of a heraldic cross patée The shape of the diffuse crosses is thought to arise from the range of wave lengths present during the early stage of the decomposition. The Fourrier spectrum of the modulated crystal (i.e. the diffuse intensity of the cross patée) has two components; a) the radial component describing the range of initial wave lengths and b) the tangential component describing the range in orientation of the waves[29]. We have found that the arms of the cross patée are aligned parallel to the cube directions and that the range of orientations of the wave vector β (the tangential component of the Fourrier spectrum)

gradually decreases during aging. Cahn[32] has shown that in cubic crystals, the introduction of an elastic energy term in the diffusion equation favors the formation of {100} plane waves if the elastic constants are anisotropic, and if $2\,C_{44} > C_{11} + C_{12}$. It is believed that it is the increase in the anisotropic elastic energy[29] during the decomposition that causes a decrease in the radial component of the Fourrier spectrum, which is illustrated by the decrease in the radial component of the diffuse intensity in diffraction patterns of Fig. 4.

After a very short aging time, the exponential dependence of the amplitude on $R(\beta)$ in equation (2) is expected to cause a dominance of components with wave numbers clustered about β_m[25,26,27]. This is well shown in Figs., 4(a) and (b) for the alloys 0.5 and 0.8 respectively where discreet "side band" satellites gradually emerge from the continuous diffuse intensity of the cross paterns.

5.3 The Growth Stage

After short aging, a gradual increase occurs of the wave length of the dominant modulation λ_m. This is illustrated in the sequence of micrographs in Fig. 6 for the symmetrical alloy 0.5. Correspondingly, the spacing of <100> satellites in diffraction patterns gradually decreases with aging (see Fig. 4). The kinetics of growth of λ can be best expressed by $\lambda \alpha kt^n$ where the exponent n was found to be temperature dependent ($n = 0.127$, 0.172 and 0.216 at 200°, 240° and 300°C).

The time dependence of the growth is weaker than that predicted by the theory of coarsening ($n = 1/3$)[20,21]. The spinodal structure in Cu-Ni-Fe alloys, and precipitates in Ni-Al alloys were found to coarsen

at a $t^{1/3}$ rate[18,22]. Our results do not support particle coarsening during the early and intermediate stages of decomposition. However, they are in agreement with the thecretical prediction of Cahn[29] that the wave lengths gradually shift toward longer wave lengths. The variation of n with temperature can be explained by enhanced growth of λ_m caused by a) the decreasing importance of the Ll_0 phase discussed in Paper II or b) the increasing importance of magnetic aging with increasing aging temperature. The latter mechanism is further discussed in the following paragraphs.

Occasionally, additional weak diffuse (110) satellites are observed in diffraction patterns (e.g. alloy 0.5 aged at 200°C for 8 min. in Fig. 4). These (110) satellites are not observed if the alloy is aged for shorter or longer times. Similar (110) satellites were observed by Tiapkin and Jibuti[28] in Fe-Be alloys. Their calculations showed that for a square composition modulation, the intensity of the (110) satellites increases with the misfit $\Delta a/a$ and the wave length λ, and that their intensity is greater than that of the (100) satellites for misfits larger than 3.2% or for $\lambda \geq 190$Å. The presence of (110) satellites in Cu-Mn-Al alloys cannot be explained on the basis of the model of Tiapkin and Jibuti since we observe the (110) satellites at typical values of $\Delta a/a < 2\%$ and $\lambda \simeq 50$Å.

Double diffraction does not explain the (110) satellites since their intensity would be expected to increase with increase in intensity of the (100) satellites, which is contrary to our observations. It is believed that the (110) satellites illustrate the presence of (110) compositional harmonic distortions also predicted by Cahn[29]. However,

these (110) modulations were not resolved in bright field images. Low angle x-ray data of powder sample may be difficult to interpret since the contribution of these (110) satellites to the diffuse intensity is near the radial position of the (100) satellites in reciprocal space.

Our results show that during aging of the alloy 0.5 at 200°C, the three <100> directions of growth are equally favored, whereas at 300°C (a temperature closer to the miscibility gap), there exists a preferential growth along one or two directions (e.g. Fig. 5). It has been suggested[33] that this effect may arise from the influence of the small magnetic field generated by the heating elements inside the oven during aging. This is possible since the aging temperature (300°C) is close to the Curie temperature of the Cu_2MnAl component (T_c = 360°C[34,35]. Furthermore, Cahn[36] has shown that magnetic aging inside the miscibility gap has a pronounced effect on the alignment of the particles. This effect is strongest when T_c is near the spinodal temperature T_s and when aging is carried out just below T_c and T_s[36].

5.4 Coarsening

The coarsening of the microstructure proceeds with increases in λ during aging. In the symmetrical alloy 0.5, the decomposition produces coherent rod-like particles with their long axes parallel to <001> directions (e.g. Fig. 10). In the asymmetrical alloys 0.8 and 0.9 the decomposition produces plate-like particles of the minor Cu_3Al-rich phase lying in {100} planes (Fig. 11). In the symmetrical alloy, the direction of the rods corresponds to a direction of best fit between the Cu_3Al-rich and the Cu_2MnAl-rich particles[37]. This is accomplished by a tetragonal distortion of the Cu_3Al-rich particles prior to the loss of coherency

{See Fig. 13(a) and 14(a)}. A similar tetragonal distortion prior to the break of coherency in Cu-Ni-Fe alloys was reported by Butler and Thomas[18]. In the asymmetrical alloys, the plate-like morphology of the Cu_3Al-rich minor phase reflects the best fit between the Cu_3Al-rich particles and the Cu_2MnAl matrix in two orthogonal directions in the flat face of the particles[37] prior to the loss of coherency.

The striking feature of the coarsening in the symmetrical alloy (See Fig. 10) is the presence of wave lengths of about 2,000Å often separated by regions having a much smaller modulation ($\lambda \simeq 200$Å). This shows that once coherency is lost, the coarsening cannot be expressed in the form of $\lambda \alpha kt^n$. For that reason, no λ larger than 200Å was plotted in Fig. 8. Similar results were obtained in spinodally decomposed Cu-Ni-Fe by Butler and Thomas[18]. The accelerated coarsening can be attributed to the increased rate of relief of interfacial strain resulting from the generation of interfacial dislocations. However, the present results show that in the 0.5 alloy aged at 300°C, the wave lengths can vary by more than one order of magnitude within one wave length of the larger modulation. This cannot be explained by the faster growth of semicoherent particles since interfacial dislocations were not observed in this and thick areas of the foils.

The coarsening model that best fits our results is that proposed by Swanger et al.[30]. Their computer simulations have shown the influence of the gradient energy term in the solution of the non-linear diffusion equation (see Section 5.1). They consider four stages during the growth of the modulations. It appears that when the amplitude of sinusoidal modulations approaches the spinodal boundary, the importance

of the gradient energy term increases especially near the interface and causes preferential growth of the amplitude which results in the squaring of the modulation. This corresponds to stage 1 and 2. During stage 3, tne composition of the corners (near the interface) crosses the spinodal boundary which results in a "convoluted structure" where small modulations superimposed on to the large initial modulations. Particle coarsening occurs during stage 4. It is suggested that the development of the coherent microstructure in the alloy 0.5 can be similarly interpreted. An increase in the composition gradient favors the growth of the small wave length modulation by increasing the gradient energy term in the non-linear diffusion equation. The lever rule is obeyed by the generation of amplitudes of the "opposite" composition and also by the slower crossing of the spinodal boundary by the plateau where the gradient energy term has little favorable influence. Eventually, particle coarsening occurs as illustrated by the absence of small wave lengths in the alloy 0.5 aged at 300°C for 7,000 min. or longer.

It is not clear why the interface of the small modulations does not lose coherency before coarsening. This would reduce the interfacial energy which is highly localized in the regions containing the small modulations. However, interfacial dislocations were not observed in the thick areas of the foils where part of the interface was retained.

5.5 Loss of Coherency

Our results have shown that the alloy 0.5 loses coherency at wave lengths larger than 2,000Å. There are two mechanisms for the loss of coherency in this alloy; a) the generation of interfacial plate-like precipitates (see P in Fig. 12) and b) the generation of 1/2a<100>

edge dislocations[24].

In the non-symmetrical alloy 0.8 and 0.9, Fig. 15 shows no precipitation at the planar coherent interface and the early stage of the loss of coherency can be studied. We have observed interfacial dislocations and an accelerated thickening of the plate-like particles in the vicinity of the dislocated regions of the interface (e.g. at x in Fig. 15). This observation suggests that interfacial dislocations increase the growth rate of the particles at least in the non-symmetrical alloys.

After loss of coherency, both phases have a cubic structure and the volume of the unit cell of the Cu_2MnAl-rich component is related to that of the Cu_3Al-rich component by the expression

$$V_{Cu_2MnAl} = V_{Cu_3Al}(1 + \delta)^3$$

where δ, a fractional dilation of the lattice, is a function of composition which in turn is a function of the decomposition temperature. If these two phases were coherent, the state of the coherency strain at the interface would be purely dilatational. However, before loss of coherency, the lattice parameter is the same for both phases in the direction of the long axis of the particle; and therefore, there is no strain in this direction. This produces the metastable tetragonal structure in the Cu_3Al-rich phase and minimizes the elastic energy at the coherent interface. When coherency is lost, the interfacial dislocations must relieve the dilatational strain at the interface for the correct matching of the lattice planes of the adjoining cubic phases. In smoothly curved interfaces, this is best accomplished by a network of three orthogonal sets of parallel edge dislocations having Burgers vectors of the type $a/2\langle 100\rangle$[24].

If the interface plane is (001), the two sets of dislocations 1/2a[100] and 1/2a[010] relieve the interfacial strain (see Fig. 12).

The values of $\Delta a/a$ given in Table 2 are somewhat lower than the value of 2% calculated from the Cu_3Al and Cu_2MnAl lattice parameters[8,10,11]. This is believed to reflect a compositional change between the two phases in the alloy 0.5 aged at 300°C that is smaller than that represented by Cu_3Al and Cu_2MnAl. The micrographs obtained after prolonged aging of the alloy 0.5 at 300°C suggest an equal volume fraction of the two phases (see Fig. 10 and 12). However, the expected volume fraction of the Cu_2MnAl-rich phase at 300°C by the application of the lever rule to the miscibility gap in Fig. 2 is closer to 66% rather than the observed 50%. This may be explained by a rotation of the decomposition tie line with respect to the Cu_3Al-Cu_2MnAl tie line of the alloys studied[38]. In fact overaging of the alloy 0.5 at 300°C results in further transformation of the two cubic phases in a manner which suggests decomposition along the Cu_9Al_4-$Cu_{2.2}MnAl_{0.8}$ tie-line. The evidence for the rotation of the decomposition tie-line will be given in paper III.

5.6 Nucleation and Growth of Cu_2MnAl-rich Particles

Evidence of decomposition by the nucleation and growth mechanism inside the miscibility gap was found in the asymmetrical alloy 0.2. The composition of this alloy lies near the binary end of the miscibility gap, and its decomposition produces rows of cubes of the Cu_2MnAl-rich phase parallel to the cube axis of the Cu_3Al rich matrix (see Fig. 17). In the briefly aged alloy, it was found that the heterogeneous precipitation occurs almost entirely at the large 1/4a<111> APB's and possibly at the smaller 1/2a<100> APB's. This is well illustrated in Fig. 16 showing the

heterogeneously nucleated precipitates in a) the 1/4a<111> APBs in b) and both the 1/4a<111> and the small 1/2a<100> APBs in c). Swann[39] also observed the heterogeneous precipitation of a γ-type phase at both types of APBs in a Cu-Ni-Al alloy having the DO_3 structure and he suggests that the driving force for mucleation comes from the APB energy itself. We have studied the annihilation characteristics of both types of APBs during aging inside the microscope, and details will be published elsewhere. We found that in alloy 0.5, the energy of the 1/4a<111> APBs is 25% larger than the energy of the 1/2a<100> APBs. This is consistent with our observation that the B2 ordering temperature T_cB2 is higher than T_cL2_1-DO_3 in alloys studied during the present investigation. It is therefore energetically more favorable to form stable nuclei of the precipitated phase at 1/4a<111> than at 1/2a<100> APBs.

In contrast to the nucleation and growth behaviour of the asymmetrical alloy 0.2, no heterogeneous precipitation at APBs was observed in alloys aged well inside the miscibility gap. This is illustrated in the (111) dark field micrograph of Fig. 9 showing both the anisotropic composition modulation and the isotropic 1/2a<100> APBs. This typical microstructure is consistent with the spinodal mechanism.

6. SUMMARY

1. The alloys along the composition tie-line Cu_3Al-Cu_2MnAl were found to order during the quench to an ordered solid solution based on the DO_3 structure of Cu_3Al and the $L2_1$ structure of Cu_2MnAl.
2. Isothermal aging of the alloys at temperatures below 350°C results in the decomposition of the alloys inside a miscibility gap into modulations rich in Cu_3Al and Cu_2MnAl. It is suggested that the shape of the

miscibility gap is asymmetrical along the composition line of the alloys studied.

3. The early stages of the decomposition possess all the metallographic characteristics of a spinodal transformation. The decomposition is first detected in diffraction patterns by the formation of diffuse scattering in the shape of an heraldic cross patée around all reflections. During further aging well defined satellites emerge from the diffuse intensity and the intersatellite spacing decreases as the aging time increases. At this stage, <100> composition modulations are observed in electron microscope images. In the alloy $Cu_{2.5}Mn_{0.5}Al$, the gradual increase of the compositional wave length is characterized by a $\lambda \alpha t^n$ law where n was found to be 0.127, 0.172 and 0.216 at 200°C, 240°C and 300°C respectively.

5. Further aging produces coherent rod-shape particles parallel to the <100> directions in the alloy $Cu_{2.5}Mn_{0.5}Al$ and coherent plate-like particles parallel to the {100} planes in the ternary rich $Cu_{2.2}Mn_{0.8}$ and $Cu_{2.1}Mn_{0.9}Al$ alloys.

6. In $Cu_{2.5}Mn_{0.5}Al$ alloy, the Cu_2MnAl-rich rod shape particles have a cubic structure whereas those rich in Cu_3Al have a tetragonal structure.

7. The coherent microstructure of $Cu_{2.5}Mn_{0.5}Al$ consists of a compositional wavelength of about 2000Å, often separated by small regions of λ = 200Å.

8. During further aging of the alloys, the coherency strain is relieved primarily by the generation of interfacial dislocations of the type a/2<100> and the two phases then have cubic structures.

9. The semi-coherent microstructure of the alloy $Cu_{2.5}Mn_{0.5}Al$ shows an equal proportion of the two phases. This suggests that this alloy is

situated near the center of the miscibility gap. Furthermore, the Cu_3Al-rich phase possess a "tweed-like" texture indicating that it contains a high density of fine coherent particles, or is itself modulated.

10. In the $Cu_{2.8}Mn_{0.2}Al$ alloy aged at 240°C, the Cu_2MnAl-rich phase heterogeneously precipitates at $a/4_2$<111> type APBs inherited during the quench.

ACKNOWLEDGMENTS

This work was sponsored by the Atomic Energy Commission through the Lawrence Berkeley Laboratory. M. B. gratefully acknowledges receipt of a fellowship by Hydro-Quebec and SIDBEC-DOSCO, Montreal, Canada. The line diagrams were skillfully drawn by G. Pelatowski.

REFERENCES

1. D. R. F. West and D. Lloyd Thomas, J. Inst. Metals, 85, 97 (1956-57).
2. G. B. Johnston and E. O. Hall, J. Phys. Chem. Solids, 29, 195 (1968).
3. R. Kimura, K. Endo and T. Ohoyama, J. Phys. Soc. Japan, 17, 723 (1962).
4. Y. E. G. Nesterenko, I. A. Osipenko and S. A. Firstov, Phys. of Metals and Metallography, 27, No. 1, 135 (1969).
5. J. P. Lisse and B. Dubois, Menoires Scientififues Rev. Metallurg. LXVIII, No. 7-8 (1971).
6. M. Bouchard and P. R. Swann, 7th Int. Congress Electron Microscopy, (Grenoble, 1970), Soc Française de Mic Electron., 2 475 (1970).
7. M. Bouchard and P. R. Swann, to be published.
8. A. J. Bradley and J. W. Rogers, Proc. Roy. Soc., 144A, 350 (1934).
9. K. Endo, T. Ohoyama and R. Kimura, J. Phys. Soc. Japan, 19, 1494 (1964).
10. D. P. Oxley, R. S. Tebble and K. C. Williams, J. Appl. Phys, 34, No. 4, 1362 (1963).
11. E. Persson, Z. Physik, 57, 115 (1929) (see Ref. 8).
12. R. D. Schoone and E. A. Fischione, Rev. Scientific Inst., 37, No. 10, 1351 (1966).
13. M. J. Marcinkowski, Electron Microscopy and Strength of Crystals (Interscience, N.Y. 1962) G. Thomas and J. Washburn, Eds., p 333.
14. P. R. Swann and H. Warlimont, Acta Met., 11, 511 (1963).
15. S. Kajiwara, J. Phys. Soc. Japan, 22, 3, 795 (1967).
16. L. E. Tanner, Phil. Mag., 14, 111 (1966).
17. P. B. Hirsch, A. Howie, R. B. Nicholson, D. W. Pashley and M. J. Whelan, Electron Microscopy of Thin Crystals (London, Butterworths, 1965).

18. E. P. Butler and G. Thomas, Acta Met., 18, 347 (1970).

19. R. W. Southworth and S. L. Deleeuw, Digital Computation and Numerical Methods, McGraw Hill (1965).

20. I. M. Lifshitz and V. V. Slyozov, J. Phys. Chem. Solids, 19, 35 (1961).

21. C. Wagner, Z. Electrochem, 65, 581 (1961).

22. A. J. Ardell and R. B. Nicholson, Acta Met., 14, 1295 (1966).

23. S. Amelinckx, R. Gevers, G. Remaut and J. van Landuyt, Modern Diffraction Techniques in Materials Science (North Holland, 1970).

24. M. Bouchard, R. J. Livak and G. Thomas, Surface Science, 31, 275 (1972).

25. J. W. Cahn, Trans. AIME, 242, 166 (1968).

26. J. E. Hilliard, Phase Transformations, ASM, Metals Park, 497 (1970).

27. D. deFontaine, Ultra Fine Grain Metals, Syracuse University Press, 93 (1970).

28. Yu. D. Tiapkin and M. V. Jibuti, Acta Met., 19, 365 (1971).

29. J. W. Cahn, Acta Met., 14, 1685 (1966).

30. L. A. Swanger, P. K. Gupta and A. R. Cooper, Jr., Acta Met., 18, 9 (1970).

31. L. E. Tanner, to be published in Acta Met.

32. J. W. Cahn, Acta Met., 10, 179 (1962).

33. H. Warlimont (private communication).

34. K. Endo, T. Ohoyama and R. Kimura, J. Phys. Soc. Japan 19, 1494 (1964).

35. D. P. Oxley, R. S. Tebble and K. L. Williams, J. Appl. Physics, 54, No. 4, 1362 (1963).

36. J. W. Cahn, J. Appl. Phys. 34, 3581 (1963).

37. G. C. Weatherly, Phil. Mag., 17, 791 (1968).

38. J. E. Morral and J. W. Cahn, Acta Met., 19, 1037 (1971).

39. P. R. Swann, Phil. Mag., 14, 461 (1966).

FIGURE CAPTIONS

Fig. 1. Schematic representation of the ordering sequence during the quench of the alloy $Cu_{2.5}Mn_{0.5}Al$ (vertically) and its isothermal decomposition (horizontally).

Fig. 2. The ordering temperatures $T_c(B2)$ and $T_c(DO_3\text{-}L2_1)$ and the miscibility gap of the $(Cu\text{-}Mn)_3Al$ alloys respectively determined by thermal analysis and electron microscopy.

Fig. 3. Bright field micrograph (a) and the (001) diffraction pattern (b) of the quenched alloy, $Cu_{2.5}Mn_{0.5}Al$ ($x = 0.5$) showing a "tweed-like" microstructure and in (b) diffuse streaking.

Fig. 4. Sections of (001) diffraction patterns obtained after aging the alloys $Cu_{2.5}Mn_{0.5}Al$ ($x = 0.5$) in (a) and $Cu_{2.8}Mn_{0.2}Al$ ($x = 0.8$) in (b) at 200°C for times indicated in minutes. The figure illustrates the gradual emergence of the well defined satellites from the diffuse intensity of the cross patée and the gradual decrease of the inter-satellite spacing with increasing aging time.

Fig. 5. (111) diffraction patterns of the alloy $Cu_{2.5}Mn_{0.5}Al$ ($x = 0.5$) aged at 200°C for 15 minutes (a) and at 300°C for 30 sec. (b) and showing the symmetrical distribution of satellites in (a) and its asymmetry in (b). The circled reflections are enlarged at the bottom left corners.

Fig. 6. Bright field micrographs from the alloy $Cu_{2.2}Mn_{0.8}Al$ ($x = 0.8$) aged for (a) 30 sec. (b) 1 min. and (c) 2 min. showing the gradual increase of the wavelength of the composition modulation parallel to the cube planes. Note the fringe contrast at APBs possibly due to segregation during the quench ($\vec{g} = 220$).

Fig. 7. Bright field micrograph from the alloy $Cu_{2.2}Mn_{0.8}Al$ (x = 0.8) aged at 275°C for 15 min. showing the homogeneous decomposition near a grain boundary.

Fig. 8. A log λ vs log t plot obtained from intersatellite spacing in diffraction patterns of the alloy $Cu_{2.5}Mn_{0.5}Al$ aged at 200°C, 240°C and 300°C.

Fig. 9. (111) dark field micrograph of the alloy $Cu_{2.5}Mn_{0.5}Al$ (x = 0.5) aged at 300°C for 30 sec. showing the smoothly curved 1/4a<100> APBs and the anisotropic composition modulations.

Fig. 10. Bright field micrographs of the alloy $Cu_{2.5}Mn_{0.5}Al$ aged at 300°C for 1,400 min. in (a) and 2,000 min. in (b) showing the coherent rod-like particles with their long axis parallel to the cube directions. In (a), the rods are parallel to the foil whereas in (b), they are oriented at 45° to the foil surface. In both micrographs the large modulations are often separated by small modulations.

Fig. 11. Bright field micrograph of the asymmetrical alloy $Cu_{2.2}Mn_{0.8}Al$ (x = 0.8) aged at 315°C for 180 min. showing the plate-like morphology of the coherent Cu_3Al-rich minor phase. The interface shows the symmetrical displacement fringe contrast.

Fig. 12. Bright field micrograph of the alloy $Cu_{2.5}Mn_{0.5}Al$ (x = 0.5) aged at 300°C for 10,000 min. showing the fully developed microstructure. Note the presence of interfacial dislocations and the "tweed-like" texture of the component labelled B.

Fig. 13. (100) diffraction patterns of the alloy $Cu_{2.5}Mn_{0.5}Al$ aged at 300°C for 1000 min. in (a) and 10,000 min. in (b) obtained before and after the loss of coherency respectively. Fig. 13(a) corresponds to Fig 10(a) and 13(b) correspondes to Fig. 12. The magnitude and

direction of the arrows indicates the magnitude and direction of the splitting of reflections. The interpretation of the diffraction patterns is given in Fig. 14 (see text).

Fig. 14. Schematic representation of the marked areas in Fig. 13. The splitting observed before loss of coherency in (a) is interpreted in terms of a cubic Cu_2MnAl-rich phase coherent with a tetragonal Cu_3Al-rich phase. After loss of coherency both phases have cubic structures (see b).

Fig. 15. (111) dark field micrograph of the asymmetrical alloy $Cu_{2.2}Mn_{0.8}Al$ ($x = 0.8$) aged at 315°C for 1100 min. showing partially dislocated interfaces. Note the more rapid thickening of the plates only in the dislocated regions of the interface.

Fig. 16. Sequence of micrographs of the same area of a foil from the asymmetrical alloy $Cu_{2.8}Mn_{0.2}Al$ ($x = 0.2$) aged at 240°C for 30 min. Note that the heterogeneous precipitates of the Cu_2MnAl-rich minor phase in (a) nucleate preferentially at the 1/4 a<111> APB's in (b) and possibly at the 1/2 a<100> APB's in (c).

Fig. 17. ($1\bar{1}1$) dark field micrograph of the asymmetrical alloy $Cu_{2.8}Mn_{0.2}Al$ aged at 240°C for 1000 min. showing the growth of the Cu_2MnAl-rich minor phase by the formation of rows of cubic particles parallel to <100> directions.

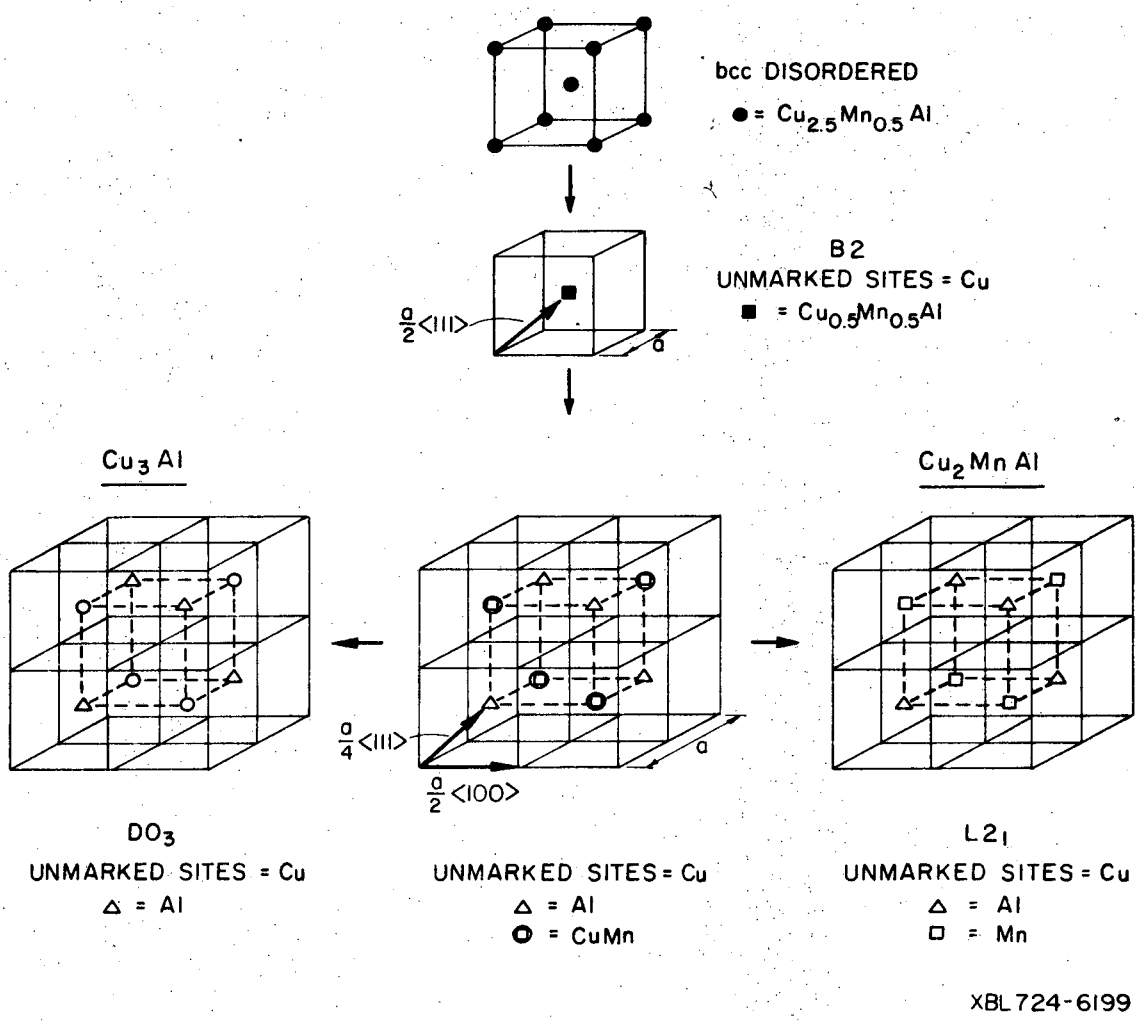

bcc DISORDERED
● = $Cu_{2.5}Mn_{0.5}Al$
B2
UNMARKED SITES = Cu
■ = $Cu_{0.5}Mn_{0.5}Al$
$\frac{a}{2}\langle 111\rangle$
a
Cu_3Al
Cu_2MnAl
$\frac{a}{4}\langle 111\rangle$
$\frac{a}{2}\langle 100\rangle$
DO_3
UNMARKED SITES = Cu
△ = Al
UNMARKED SITES = Cu
△ = Al
O = CuMn
$L2_1$
UNMARKED SITES = Cu
△ = Al
□ = Mn
XBL724-6199

Fig. 1.

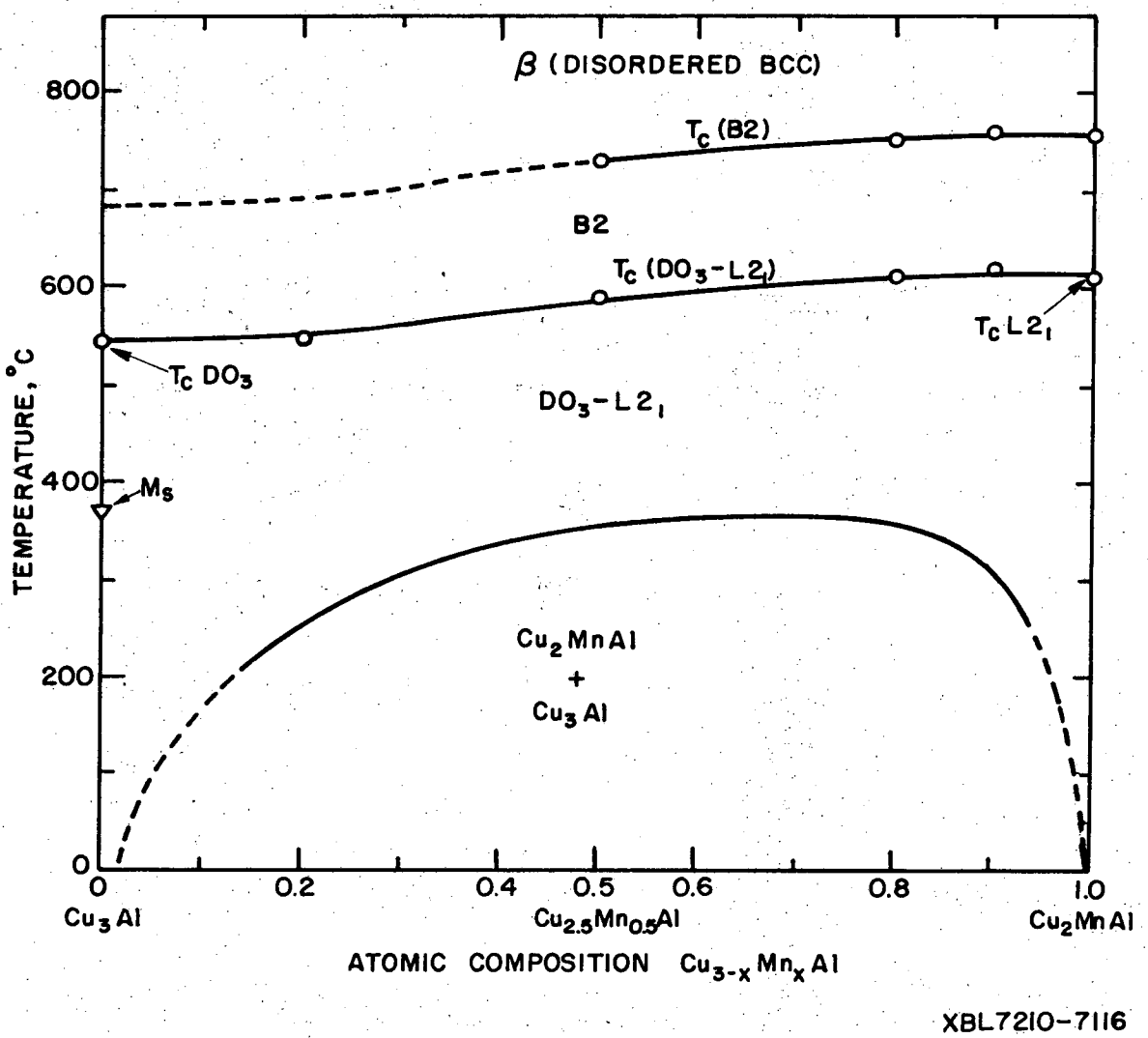
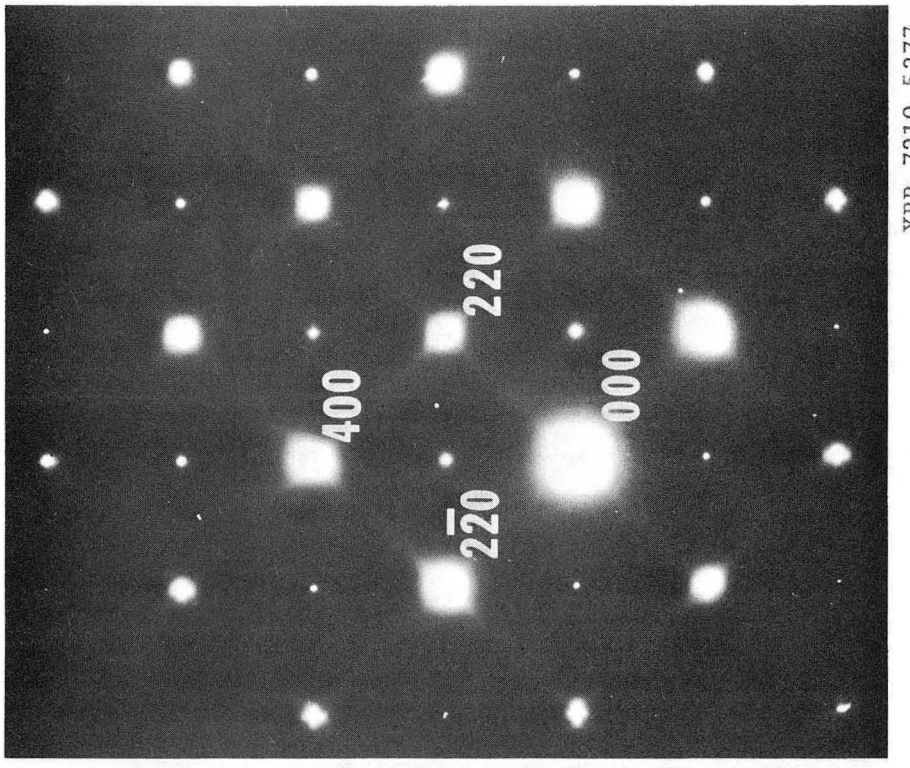

β (DISORDERED BCC)
800
T_c (B2)
B2
600
T_c (DO_3-$L2_1$)
T_c $L2_1$
T_c DO_3
DO_3-$L2_1$
400
M_s
Cu_2MnAl
+
Cu_3Al
200
0
TEMPERATURE, °C
0
0.2
0.4
0.5
0.6
0.8
1.0
Cu_3Al
$Cu_{2.5}Mn_{0.5}Al$
Cu_2MnAl
ATOMIC COMPOSITION $Cu_{3-x}Mn_xAl$
XBL7210-7116

Fig. 2.



XBB 7210-5377

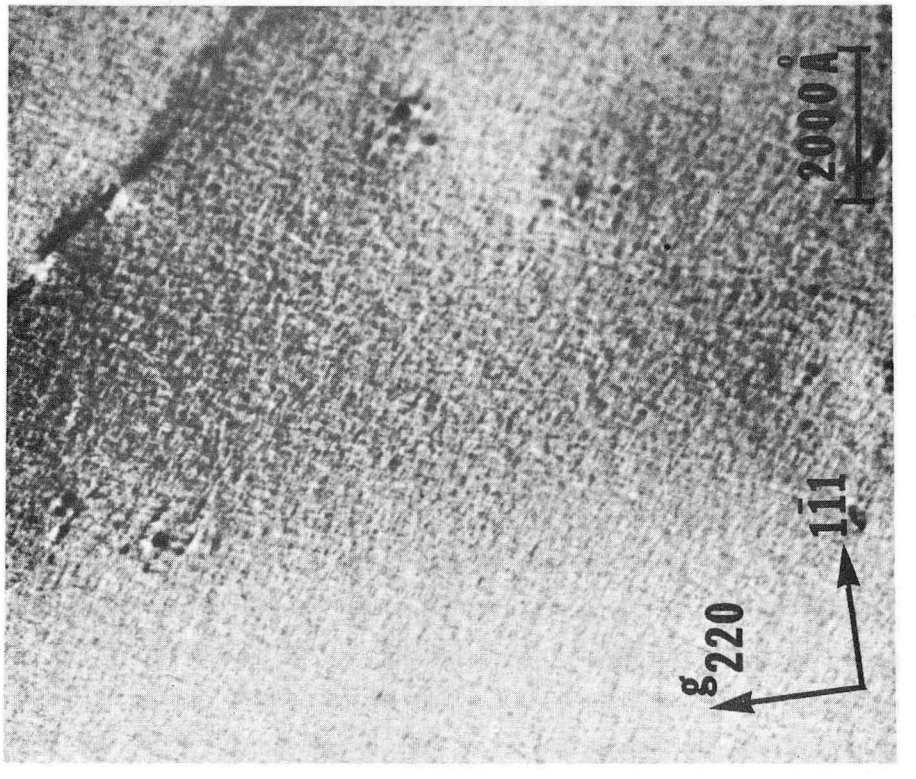


Fig. 3.

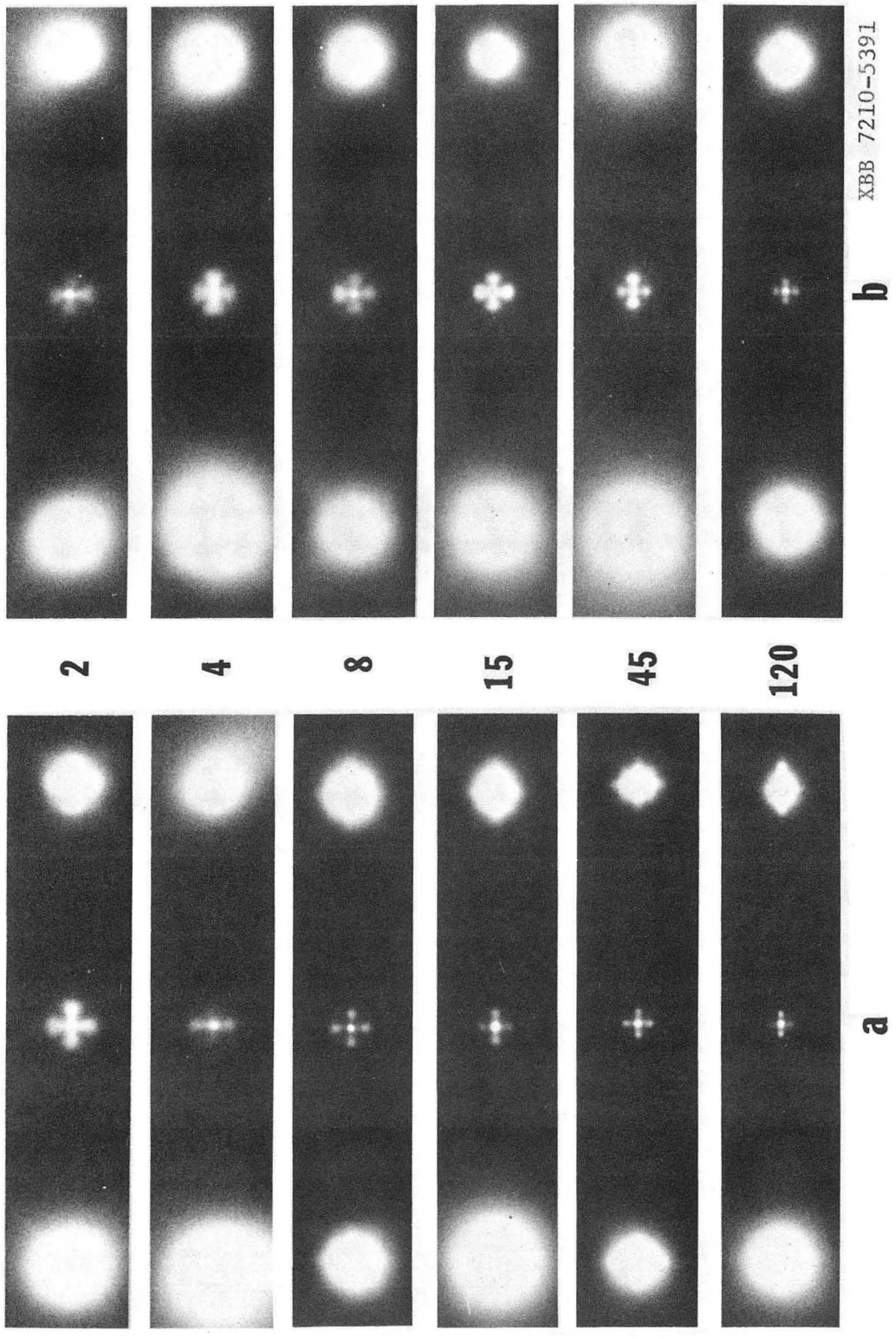
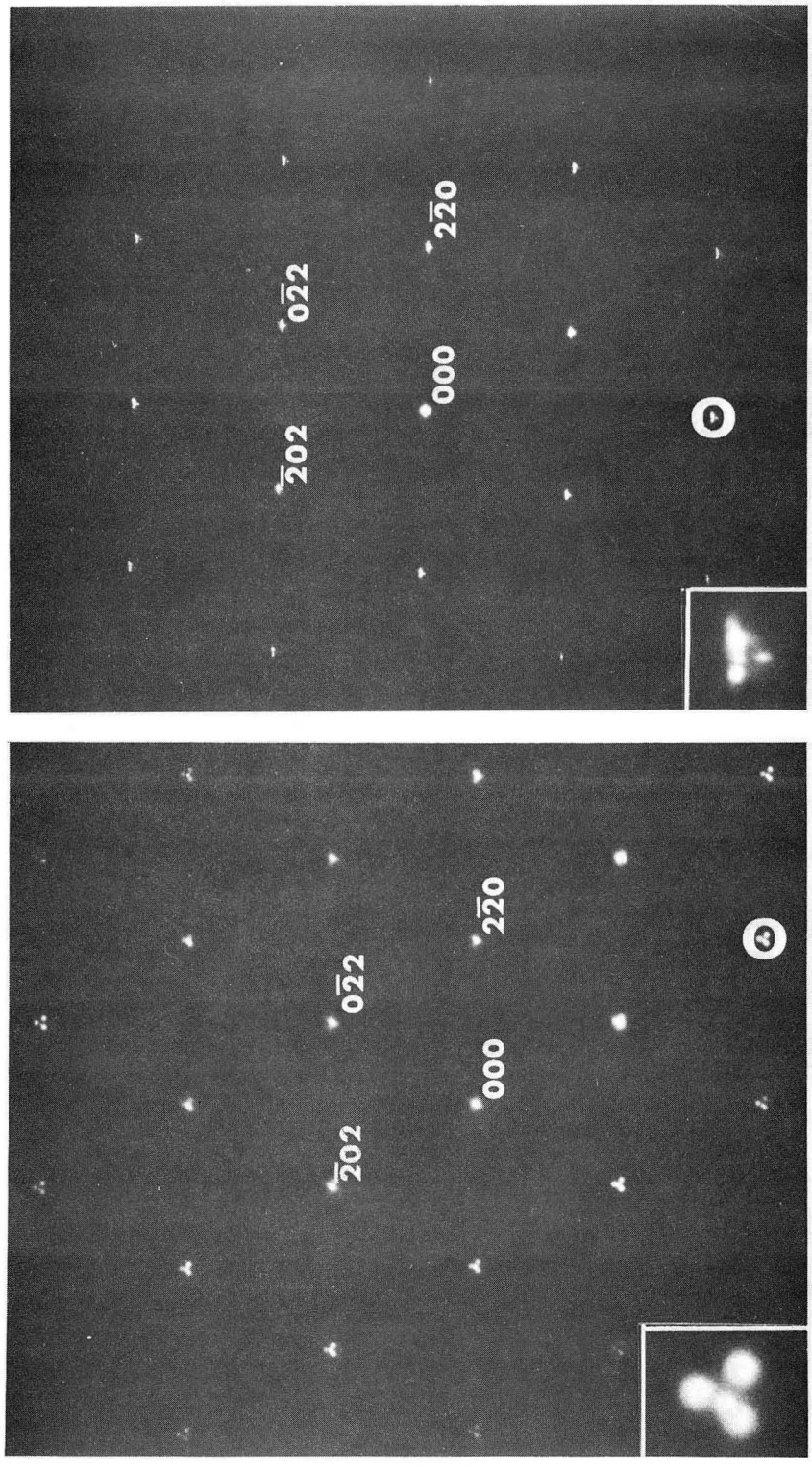


Fig. 4.



XBB 7210-5390

Fig. 5

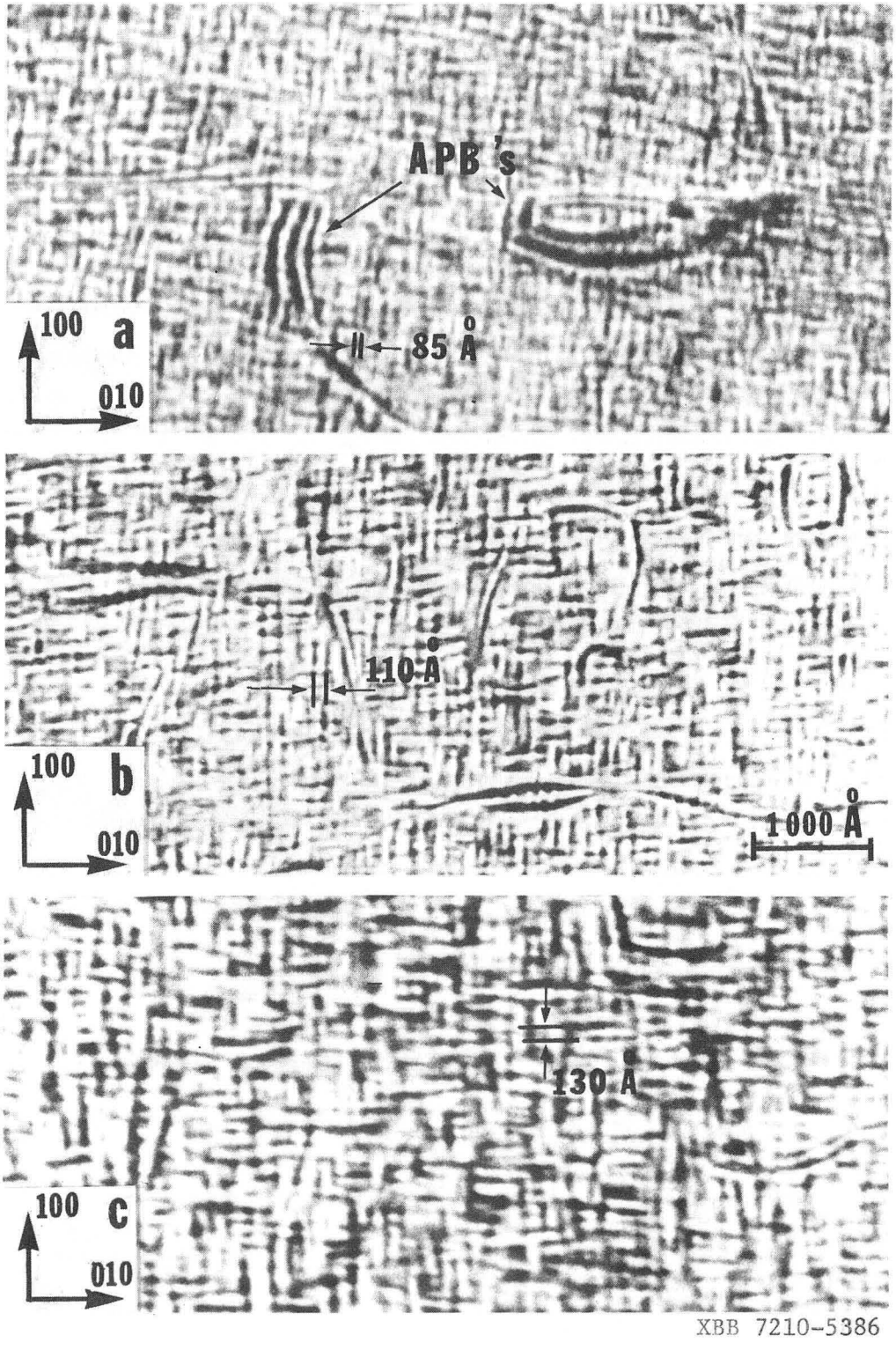

APB's
85 Å
100
a
010
110 Å
100
b
010
1000 Å
130 Å
100
c
010
XBB 7210-5386

Fig. 6.

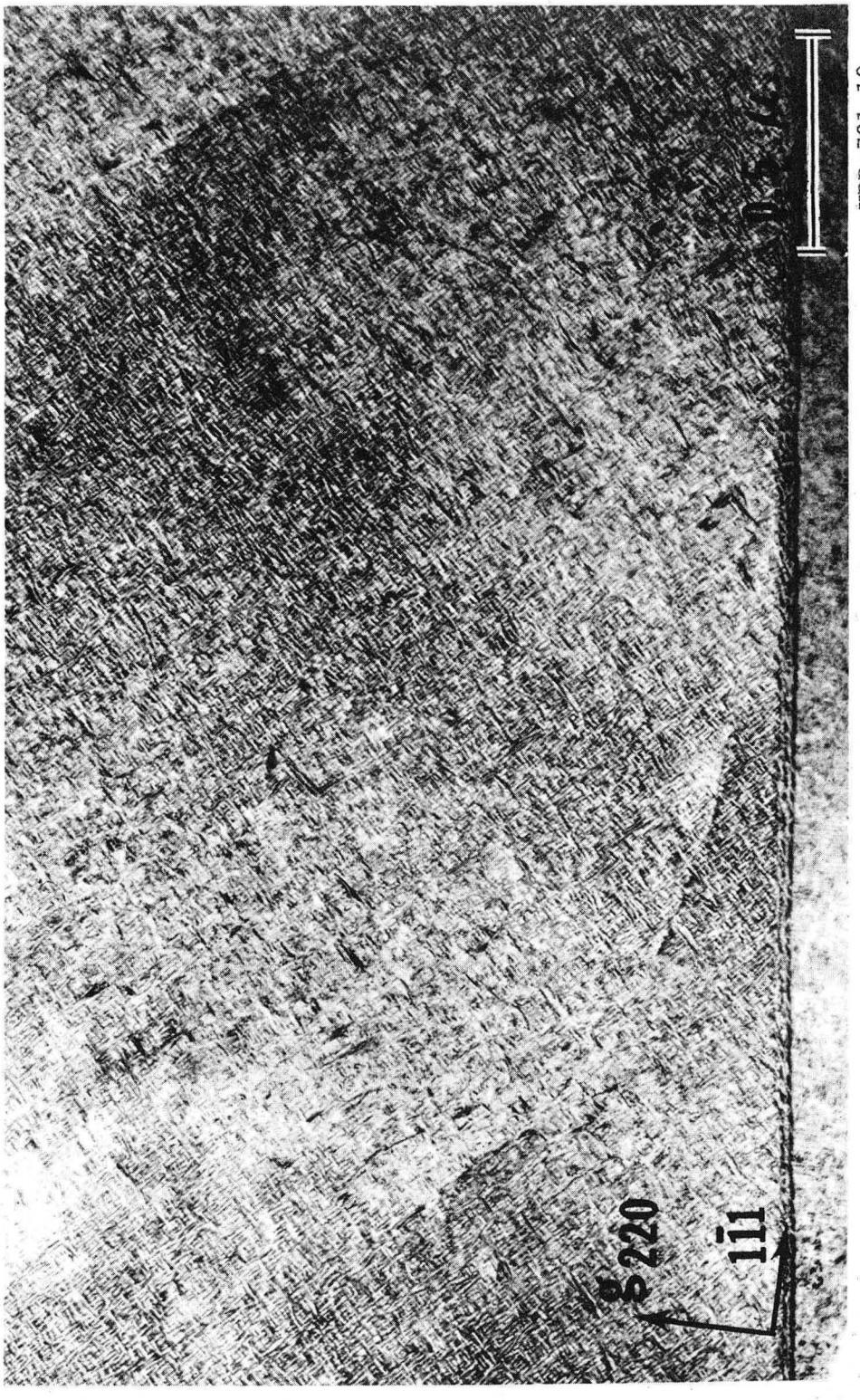


Fig. 7.

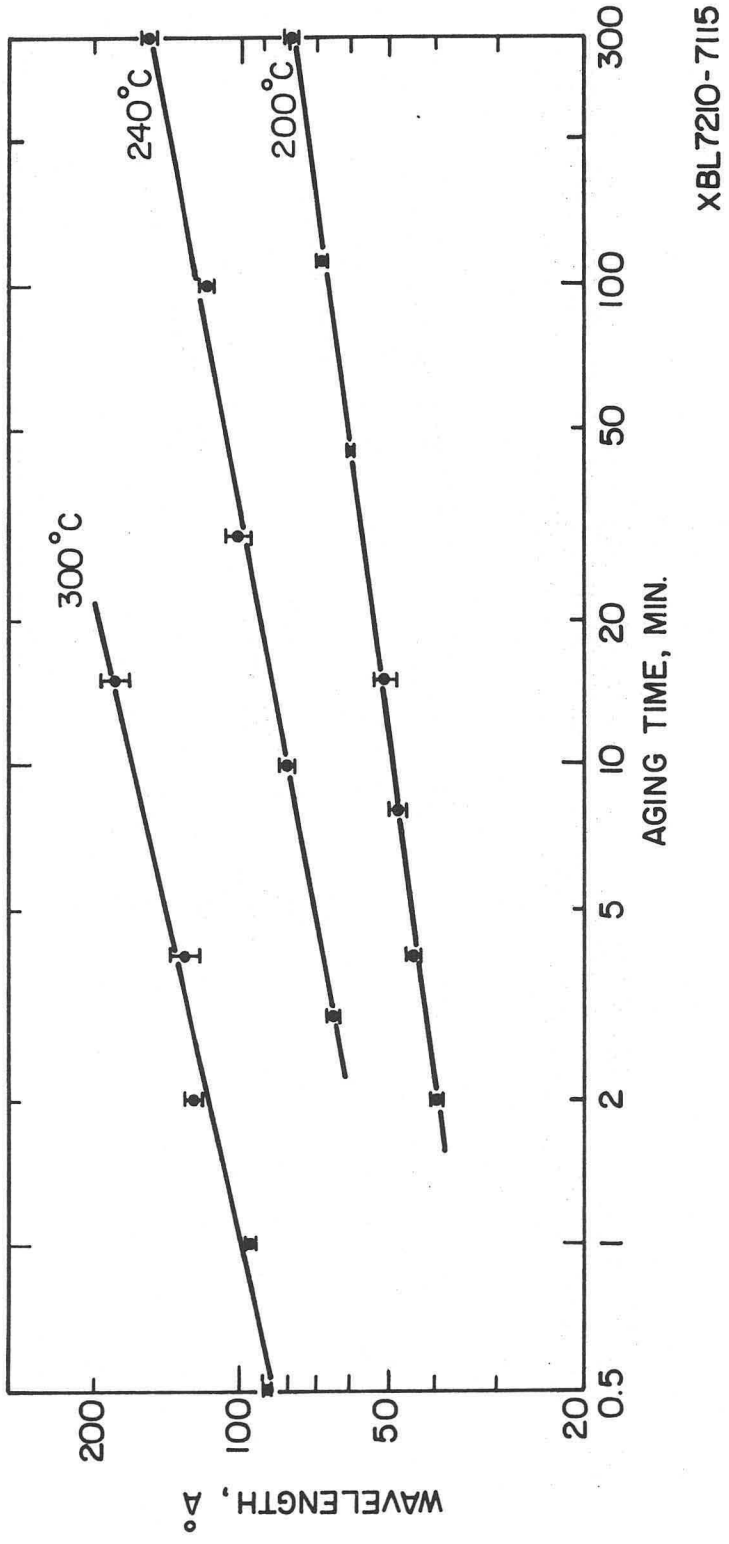
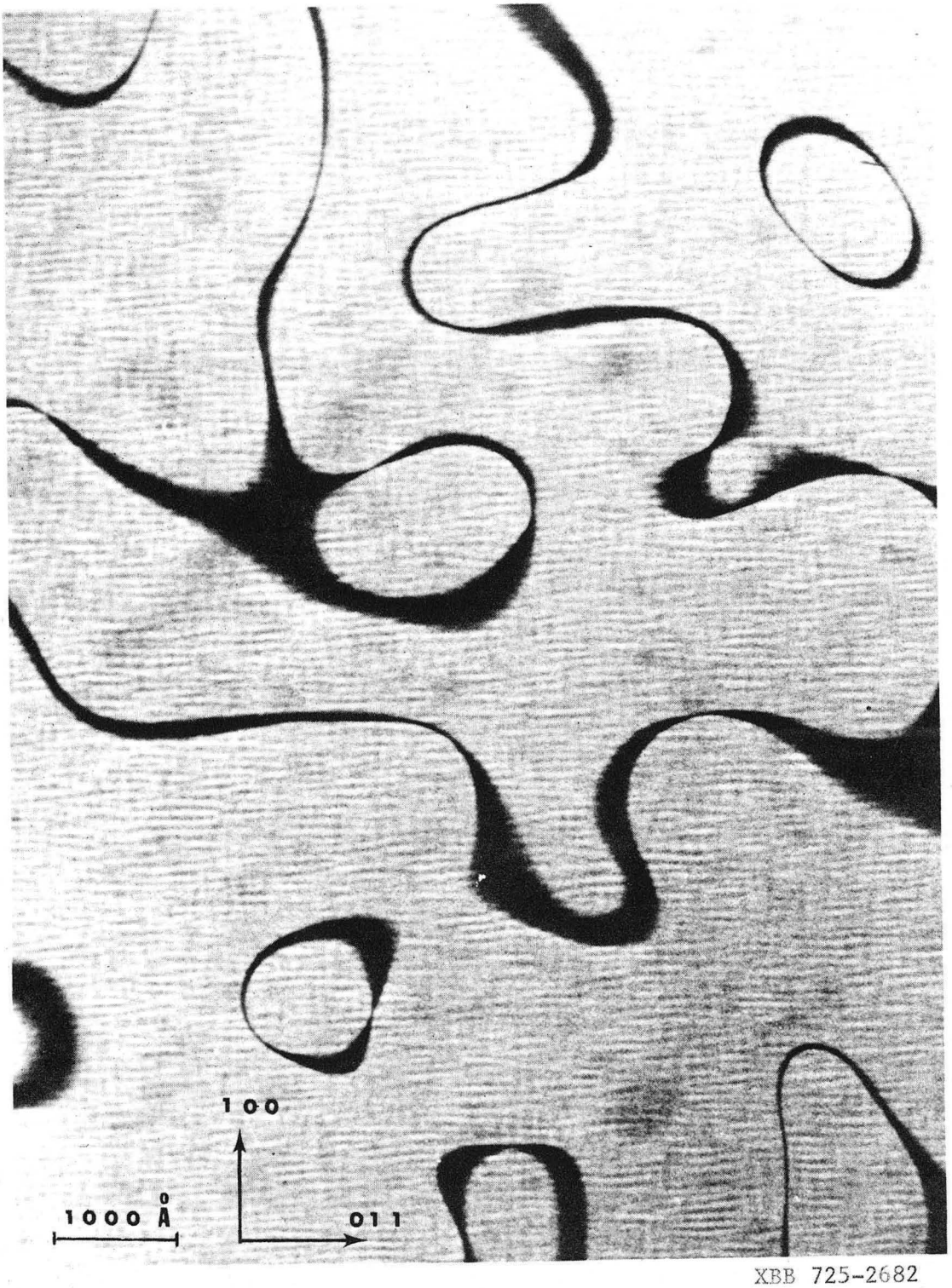

300°C
240°C
200°C
WAVELENGTH, Å
200
100
50
20
0.5
1
2
5
10
20
50
100
300
AGING TIME, MIN.
XBL7210-7115

Fig. 8.



XBB 725-2682

Fig. 9.

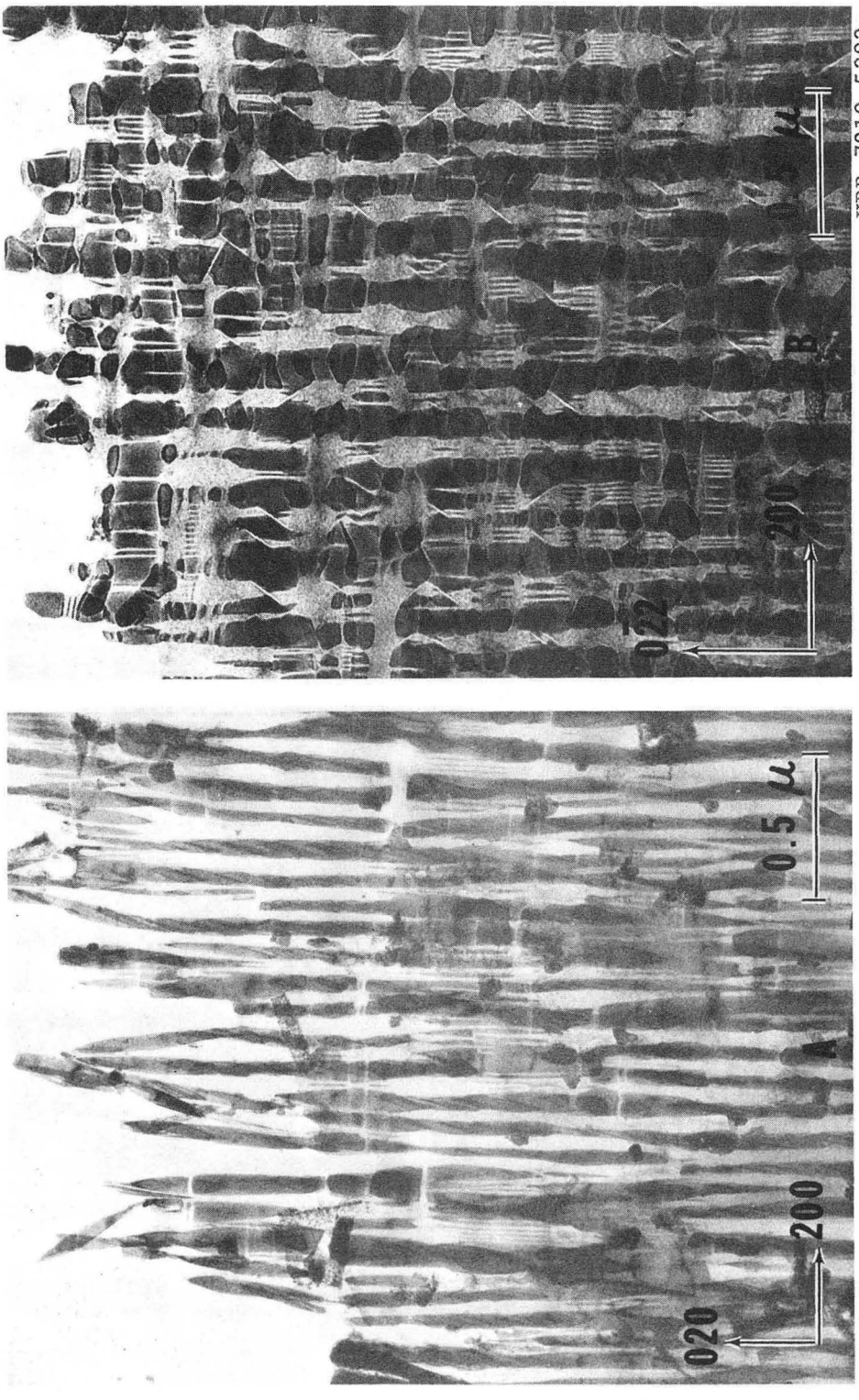
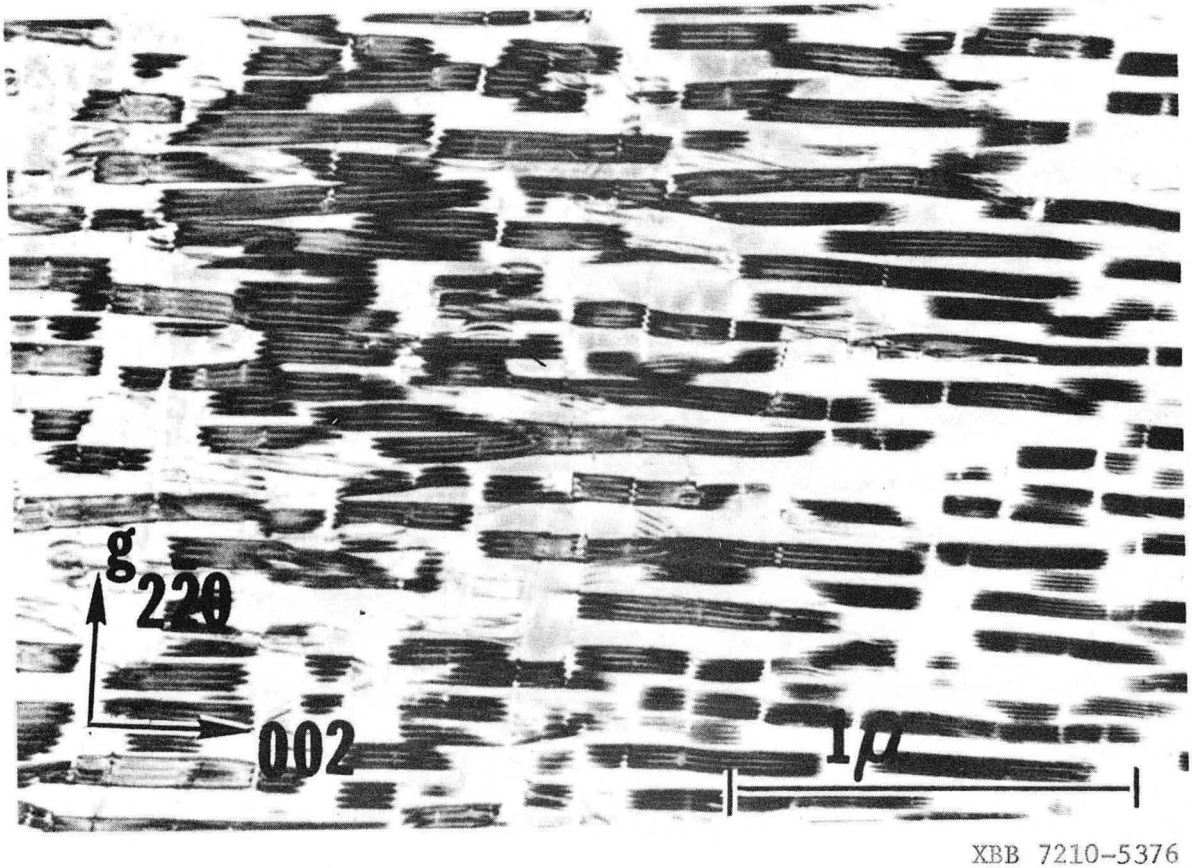
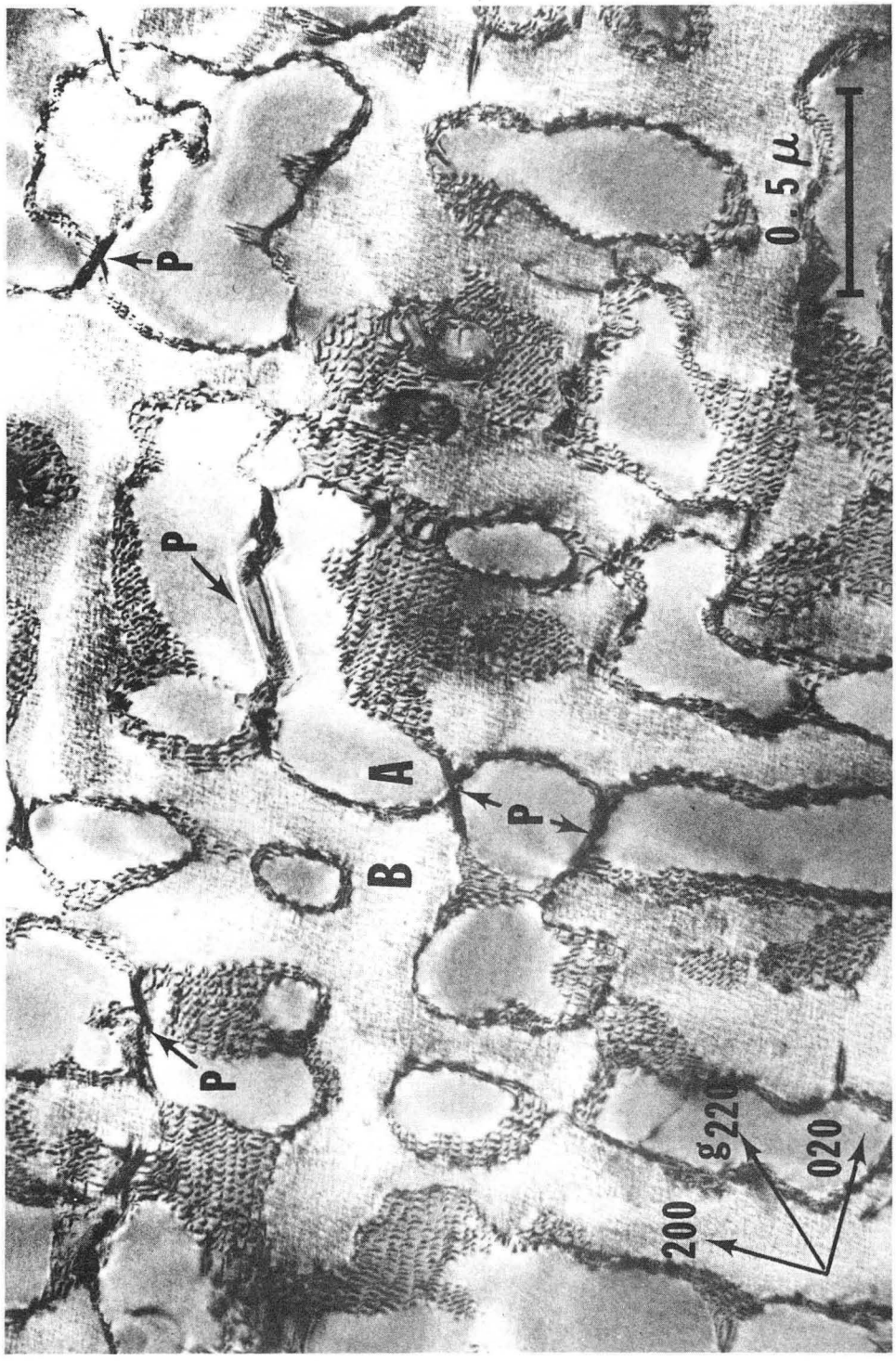


Fig. 10.



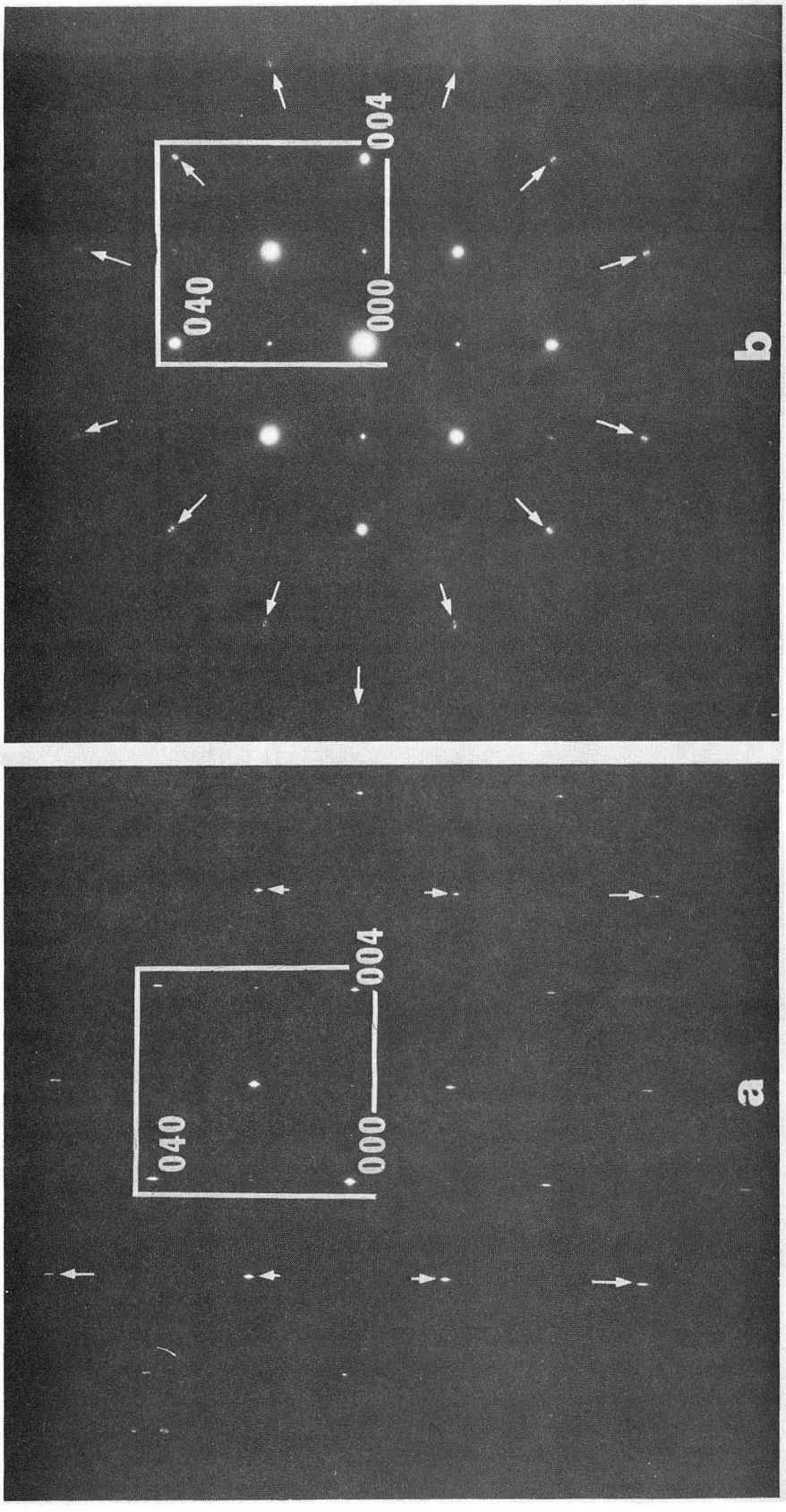
XBB 7210-5376

Fig. 11.



XBB 7210-5732

Fig. 12.



XBB 7210-5378

Fig. 13.

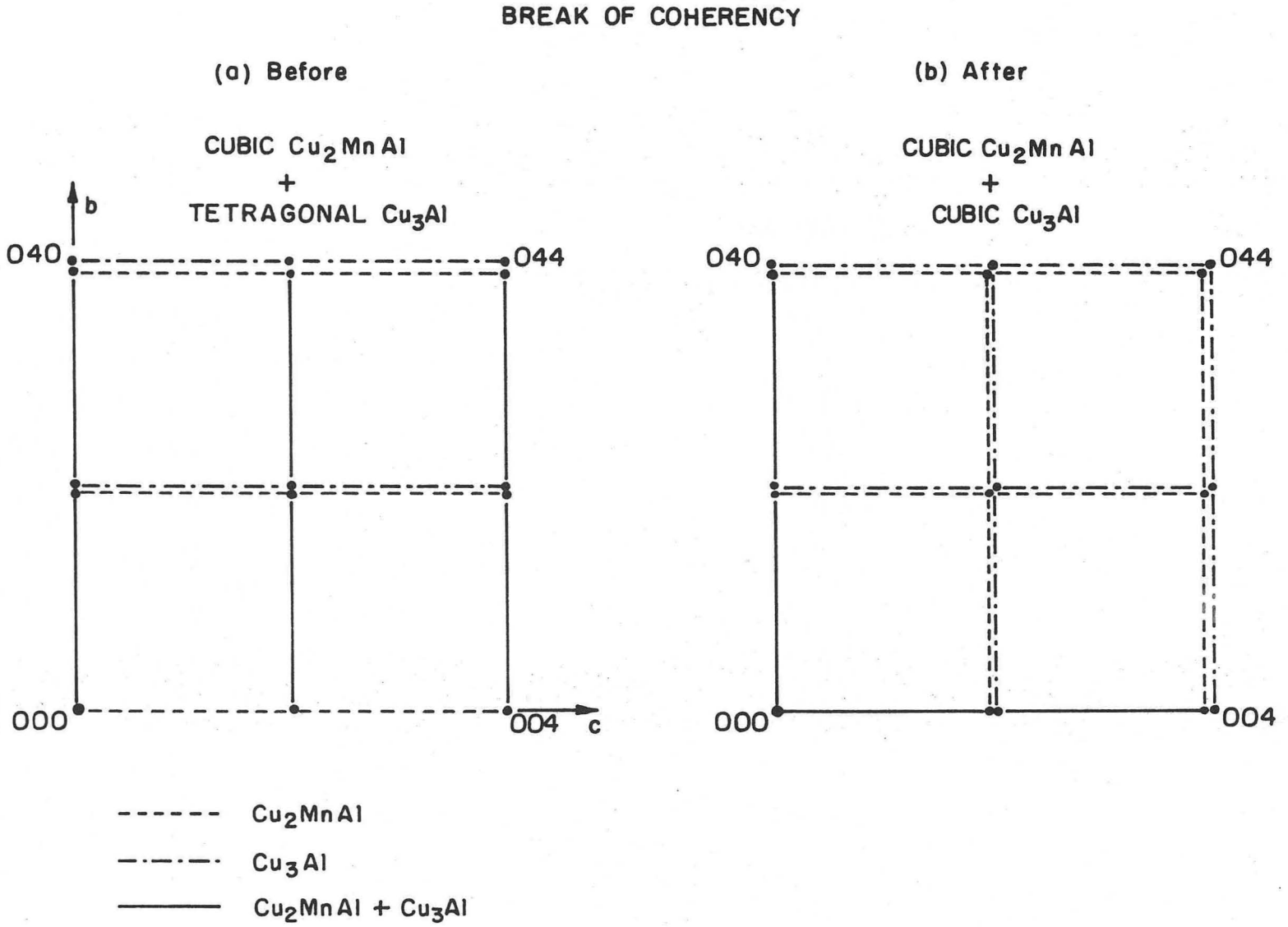
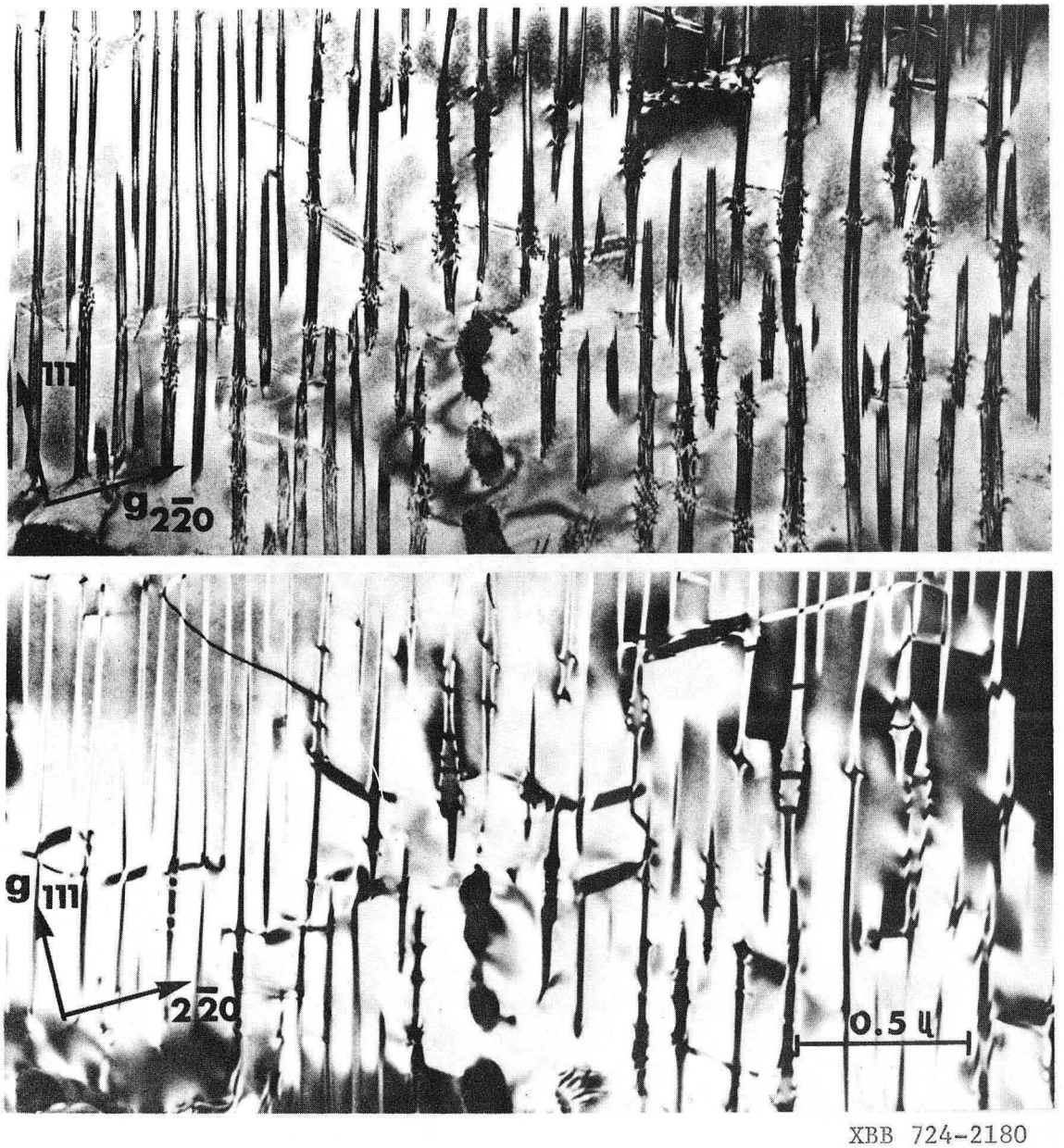
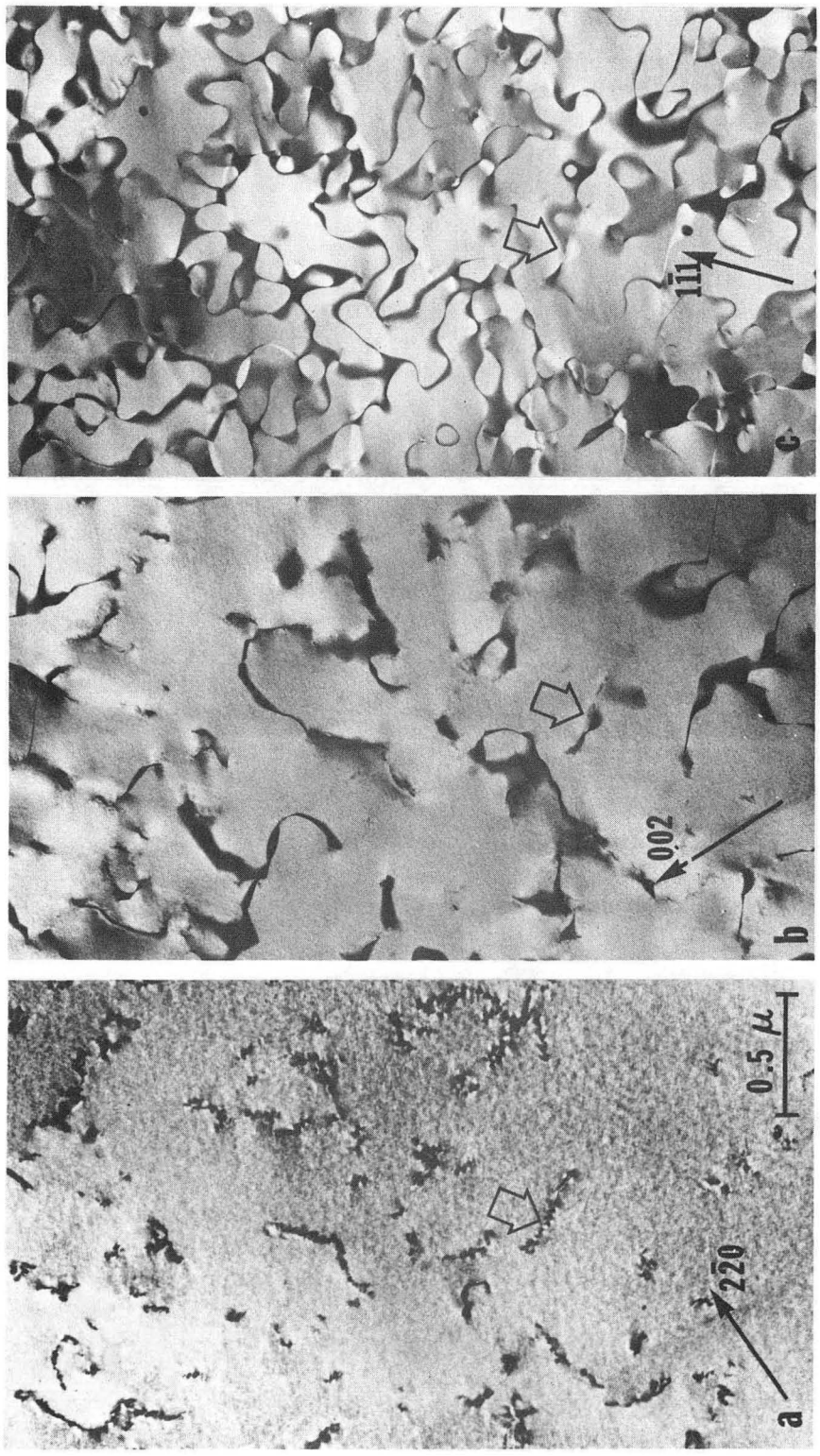

BREAK OF COHERENCY
(a) Before
CUBIC Cu_2MnAl
+
TETRAGONAL Cu_3Al
b
040
044
000
004
c
(b) After
CUBIC Cu_2MnAl
+
CUBIC Cu_3Al
040
044
000
004
Cu_2MnAl
Cu_3Al
$Cu_2MnAl + Cu_3Al$
XBL7210-7113

Fig. 14.



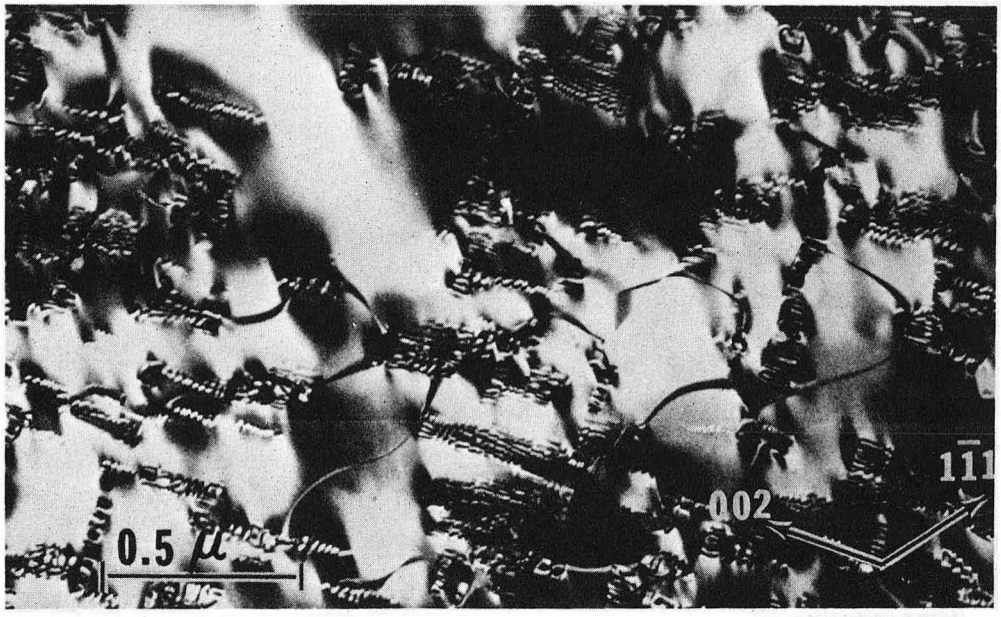
XBB 724-2180

Fig. 15.



XBB 7210-5382

Fig. 16.



XBB 7210-5381

Fig. 17.

LEGAL NOTICE

This report was prepared as an account of work sponsored by the United States Government. Neither the United States nor the United States Atomic Energy Commission, nor any of their employees, nor any of their contractors, subcontractors, or their employees, makes any warranty, express or implied, or assumes any legal liability or responsibility for the accuracy, completeness or usefulness of any information, apparatus, product or process disclosed, or represents that its use would not infringe privately owned rights.

TECHNICAL INFORMATION DIVISION
LAWRENCE BERKELEY LABORATORY
UNIVERSITY OF CALIFORNIA
BERKELEY, CALIFORNIA 94720